Journal of Petroleum Science and Engineering 218 (2022) 110918

Contents lists available at ScienceDirect

Journal of Petroleum Science and Engineering

journal homepage: www.elsevier.com/locate/petrol

The control effect of normal faults and caprocks on hydrocarbon accumulation: A case study from the Binhai fault nose of the Huanghua Depression, Bohai Bay Basin, China

Yuyang Dong [a,b], Jianhui Zeng [a,b,*], Xiongying Dong [c], Chuanming Li [a,b], Yazhou Liu [a,b]

[a] State Key Laboratory of Petroleum Resources and Prospecting, China University of Petroleum, Beijing, 102249, China
[b] College of Geosciences, China University of Petroleum, Beijing, 102249, China
[c] Exploration and Development Research Institute, Dagang Oilfield Company, PetroChina, Tianjin, 300280, China

A B S T R A C T

An exploration breakthrough was made in the Paleogene strata in the Binhai fault nose of the Huanghua Depression, but the distribution of hydrocarbons remained insufficient to understand. A series of fault-controlled traps were formed around the Gangdong fault, especially a large number of fault-block traps, which gave us a unique opportunity to use seismic data to study the distribution of the hydrocarbons under the control of normal fault and caprocks. By analysing the vertical and lateral changes of the fault throws (T-x and T-z plots), combined with the expansion index (EI), the characteristics of the Gangdong fault were studied and the evolution process of the fault was reconstructed. The fault has undergone the evolution process of lateral and dip linkage, and finally, the Gangdong fault was formed. The reconstruction of the evolution process and determination of charging stages found that the Gangdong fault was formed dip linkage just before late Neogene, providing an excellent vertical pathway for hydrocarbon migration. Besides, when the fault throw exceeds than 39 m, hydrocarbons were found near the fault, indicating a lower limit of fault throw. However, there were differences in the spatial distribution of hydrocarbons in the study area, which may be related to the integrity of the caprock. A lower thickness limit was found by analysing the relationship between the difference in hydrocarbon distribution above and below the regional caprock and the effective caprock thickness. When the effective caprock thickness is greater than this lower thickness limit, hydrocarbons can only accumulate below the caprock. When the effective caprock thickness is less than this lower limit, there is hydrocarbon accumulation above the caprock. This work highlights the evolution of normal fault and the control effect of fault-caprocks on hydrocarbon accumulation and further understands the spatial distribution of petroleum near the fault.

1. Introduction

The distribution of hydrocarbons in lacustrine basins is challenging to predict due to the evolution and activities of the faults (Xu et al., 2019; Cong et al., 2020; Wang et al., 2020, 2021). Especially for rift basins, the development of faults makes the distribution of hydrocarbons more complicated (Dasgupta et al., 2022).

Faults are critical pathways for the transportation of underground fluids (Allan, 1989; Gudmundsson et al., 2001; Ferrill et al., 2020). The fault can be a zone with a certain thickness, and the zone becomes thicker as the fault throw increases (Wibberley et al., 2008; Hansberry et al., 2021). Fault activity develops the fault damage zone, and the active fault with a larger fault throw can cause the damage zone to have relatively high permeability, thereby enhancing the transport capacity of hydrocarbons along the fault (Gudmundsson et al., 2001; Brogi, 2008; Bense et al., 2013). Through various methods, Hooper (1991) confirmed that faults have multiple active and inactive stages under the influence of tectonic movement, leading to periodic fluid flow along the fault. In addition, fault activity has been considered a potential controlling on hydrocarbon migration, destruction and reformation (Cartwright and Mansfield, 1998; Tvedt et al., 2013; Xu et al., 2016; Deng et al., 2021). A Throw-distance plot (T-x plot) can reflect the change of the fault in the lateral direction, indicating whether the fault has segmented evolution (Cartwright and Mansfield, 1998; Jackson and Rotevatn, 2013; Lathrop et al., 2021). Throw-depth plot (T-z plot) can reflect the vertical change of the fault, based on which it can be judged whether the fault has experienced dip linkage (Baudon and Cartwright, 2008a, 2008b; Cong et al., 2020). Expansion index plot (EI) can reflect the activity of the fault in different periods, and can be used to determine whether the fault is reactive (Pochat et al., 2009; Tvedt et al., 2013). These methods can be combined with other approaches to reconstruct the evolutionary history of the faults. Some studies directly link the reservoirs to the fault reactivation history and believe that fault reactivation affects the hydrocarbons distribution (Xu et al., 2016; Deng et al., 2021).

* Corresponding author. State Key Laboratory of Petroleum Resources and Prospecting, China University of Petroleum, Beijing, 102249, China.
E-mail address: zengjh@cup.edu.cn (J. Zeng).

https://doi.org/10.1016/j.petrol.2022.110918
Received 20 October 2021; Received in revised form 26 May 2022; Accepted 22 July 2022
Available online 13 August 2022

The caprock is an effective barrier to prevent fluids from migrating to the overlying strata and plays a vital role in preserving hydrocarbons (Corrado et al., 2014; Górniak, 2019; Wu et al., 2019). Since Smith (1966) proposed the concept of the sealability of the caprock and fault, scholars have begun to explore the issue of the sealability of the caprock (Watts, 1987; Schlömer and Krooss, 1997; Corrado et al., 2014; Wu et al., 2019). The current methods to evaluate the sealing ability of the caprock include high-pressure mercury intrusion, gas diffusion test, triaxial stress test and breakthrough pressure test (Krooss and Leythaeuser, 1997; Boulin et al., 2013; Kawaura et al., 2013; Arif et al., 2016). Thickness and displacement pressure are two essential factors that affect the sealing ability of the caprock. Research on caprock emphasises the integrity of the caprock, which only includes the breakthrough pressure value and rock mechanics parameters of the caprock but does not include the thickness of the caprock, and the research on the influence of the thickness on the capping property is relatively scarce (Ito et al., 2011; Schmitt et al., 2017).

The Qibei slope of the Huanghua sub-basin is located northwest of the Qikou subsag (Fig. 1B), and there have been hydrocarbon exploration breakthroughs in recent years through drilling, especially in the Binhai fault nose (Zhou et al., 2019; Zhao et al., 2020a, b). These drillings can reach a maximum depth of 4995 m, and relative shallow wells have been drilled to 3730 m. Previous studies in the Binhai fault nose emphasised the controlling role of source rick thickness, fault-sand combination, abnormally high pressure and fractures in the reservoirs in hydrocarbon accumulation (Zhou et al., 2019). In particular, the Gangdong Fault directly cuts through all the overlying strata above the crystalline basement, controlling the study region's structural characteristics and trap configuration. However, few detailed studies on the control mechanism of hydrocarbon's spatial distribution around the Gangdong fault. The existing hydrocarbons are mainly distributed on the hangingwall and footwall of the Gangdong fault, which allows us to study the relationship between fault evolutionary history and petroleum accumulation.

Here we aimed to study the characteristics of the major fault and regional caprocks and the charging time of the hydrocarbons in the Binhai fault nose to explore: (1) the lateral and longitudinal characteristics of the Gangdong fault and try to reconstruct the possible evolution of the fault; (2) the hydrocarbon charge stages of traps, determine the exact charging time; (3) the influence of fault-caprocks on the spatial distribution of hydrocarbons, exploring the possible enrichment areas of hydrocarbons. A method for evaluating the effectiveness of the caprock is proposed, which can be used for trap risk evaluation. Understanding the evolutionary history of the fault, the charging time of hydrocarbons and the control effect of fault-caprocks on hydrocarbon distribution can help avoid exploration risks and provide references for well design in the study area and other similar rift basins.

2. Geological settings

As a rift basin, the Bohai Bay Basin is located in eastern China and contains considerable oil and gas resources (Hao et al., 2009). There are six sub-basins in the Bohai Bay Basin, each of which has its own structural, sedimentary and petroleum characteristics, and the Huanghua Depression is one of them (Fig. 1A).

The Qibei slope is a typical multi-step flexural slope northwest of the Qibei subsag, situated in the west of the middle part of the Huanghua Depression (Zhao et al., 2016). The study area, Binhai fault nose, is located east of the central uplift in the Qibei slope. It is a sizeable nose-like structure attached to the footwall of the Binhai fault (fault F2 in Fig. 1C), with Gangxi bulge in the west and Qikou subsag in the east 25.0 km long and 10.4 km wide, covering a structural area of 260 km^2 (Fig. 1B). The study area is a small but hydrocarbon-rich area, with 13 wells drilled in recent years, confirming proven hydrocarbon resources of 3×10^7 t, which is an encouraging but under-explored region in the Huanghua Depression (Zhou et al., 2019). The structure is relatively simple in the western region, mainly controlled by the Gangdong fault (fault F1 in Fig. 1C), while the eastern region has a complex fault system. Under the control of the Tangjiahe Fault (fault F3 in Fig. 1C), fault F1 and the branch of fault F1, the entire eastern region presents a broom-shaped fault system (Fig. 1C). The Gangdong fault is the major fault in the study area, about 33 km long, leaning SSE, cutting through all the strata above the crystalline basement, and controlling the thickness of stratigraphic deposits and the spatial distribution of hydrocarbon resources in the study area (Zhou et al., 2019).

Following tectonic stages have developed in the Bohai Bay Basin: early syn-rift, stable rifting, fault-depressed diversionary period, thermal subsidence, and accelerated subsidence (Chen et al., 2014). The structural stages of the Qibei slope are similar to those of the Bohai Bay Basin, possessing two major stages of syn-rift and post-rift. The syn-rift contains the Shahejie Formation (Es) and the Dongying Formation (Ed), and the post-rift contains the Guantao Formation (Ng) and the Minghuazhen Formation (Nm). The study area is dominated by Paleogene-Neogene deposits, including lacustral facies, delta facies, fluvial facies and gravity flow facies. The organic-rich intervals of the Es and Ed have been generally identified as the primary source rocks on the Qibei slope (Yu et al., 2011; Wang et al., 2014), including the third member of the Shahejie Formation (Es_3), the lower of the first member of the Shahejie Formation (Es_1^3) and the third member of the Dongying Formation (Ed_3). The upper of the first member of the Shahejie Formation (Es_3^1), the middle of the first member of Shahejie Formation (Es_1^2) and the second member of the Dongying Formation (Ed_2) act as regional caprock (Fig. 2; Fu et al., 2012; Zhou et al., 2019). For the study area, the Es_1^3 is mainly composed of dark grey sandstone, siltstone and mudstone, and oil reservoirs are encountered in this formation (Fig. 3).

3. Data and analytical methods

The three-dimensional (3D) seismic data, provided by the Exploration and Development Research Institute of Dagang Oilfield Company, is used to analyse the fault throws. The depth range of the seismic data can reach 5500 ms (two-way travel time), and the distance between seismic traces is 25 m. According to the Society of Exploration Geophysicists polarity convention, black reflections in seismic data are considered positive and red reflections are negative. By applying an average velocity of 2000 m/s, the vertical resolution of seismic data is approximately 10 m.

The corresponding strata to the hangingwall and the footwall of the fault are separated by the fault, and the vertical distance between them is the fault throw, which can be calculated from the seismic profile (Fig. 4A). The throw-depth plots (T-z plots, Fig. 4B) and contoured map can be represented by the vertical change of the fault throw perpendicular to the fault strike (Baudon and Cartwright, 2008a; Duffy et al., 2015). Fault throws are obtained from 19 equally spaced seismic profiles, each of which calculated ten fault throws at different depths (Location of the seismic profiles is shown in Fig. 1C). In the T-z plots, whether the actual depth or the two-way travel time (TWT) is used as the ordinate, the variation of fault throws with depth shows similar characteristics (Tvedt et al., 2013). So in the T-z plots, the TWT was used as the ordinate to simplify the analyses. A throw-distance plot (T-x plot) can also be obtained by the calculation of fault throw, which represents the lateral variation of the fault throw in a seismic unit (Tao and Alves, 2019). The fault expansion index (EI) can be considered as the variation of the thickness ratio between the hangingwall and the footwall of a fault, and this index has been widely used to study the activity of faults in different geological history periods (Thorsen, 1963; McCulloh, 1988; Jackson and Rotevatn, 2013). When the stratum thickness of the hangingwall is greater than that of the footwall, that is, when the EI value $>$ 1.0, it indicates that the fault is active during this period of stratum deposition. On the contrary, when the EI value $\leq$ 1.0, it means that the fault is inactive.

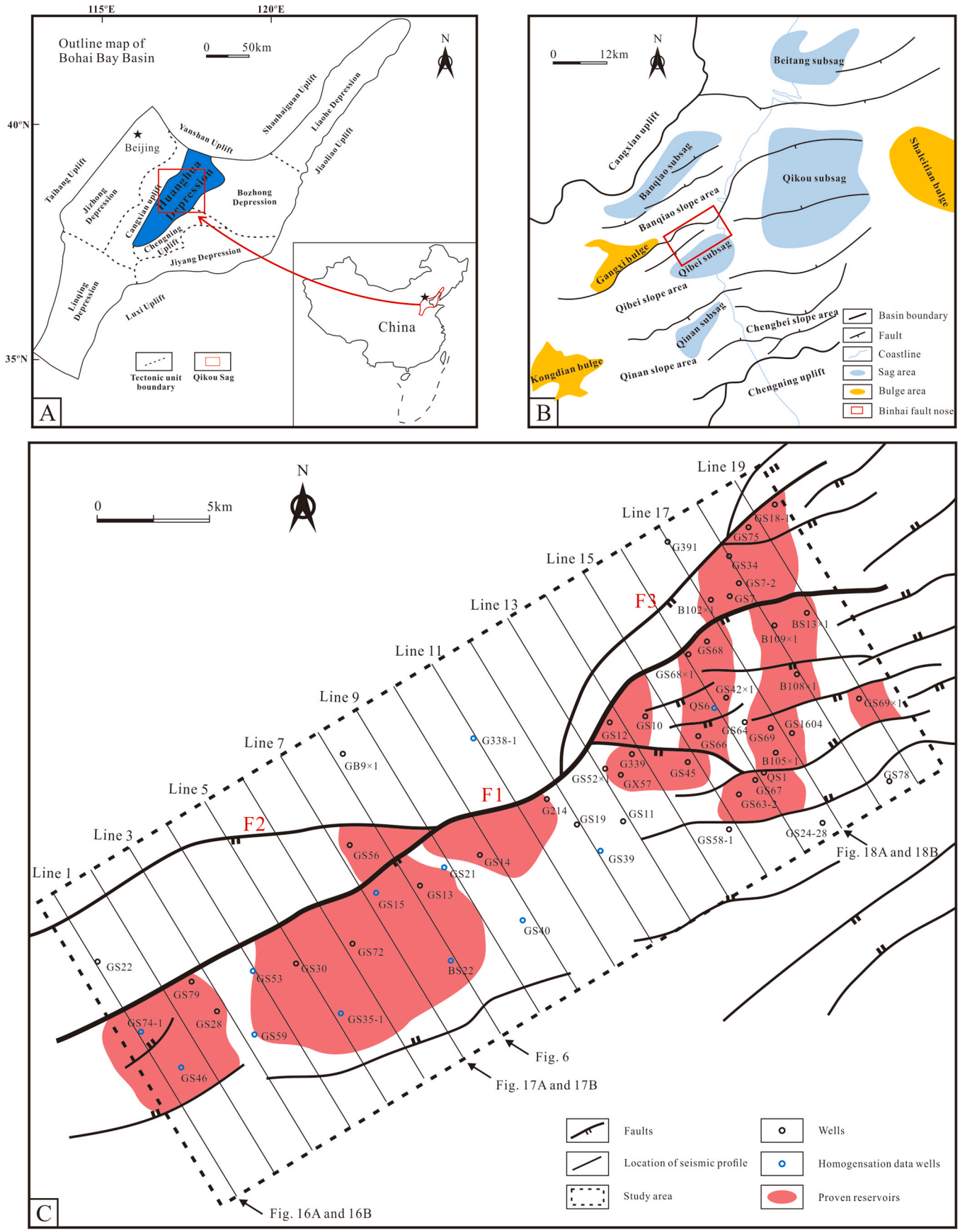

Fig. 1. (A) Location of the Huanghua Depression in the Bohai Bay Basin, eastern China. (B) Secondary structures in the Huanghua Depression, the red line shows the position of the Qibei slope. (C) The structural framework of the Binhai fault nose, the black dash line, indicates the study area. (For interpretation of the references to colour in this figure legend, the reader is referred to the Web version of this article.)

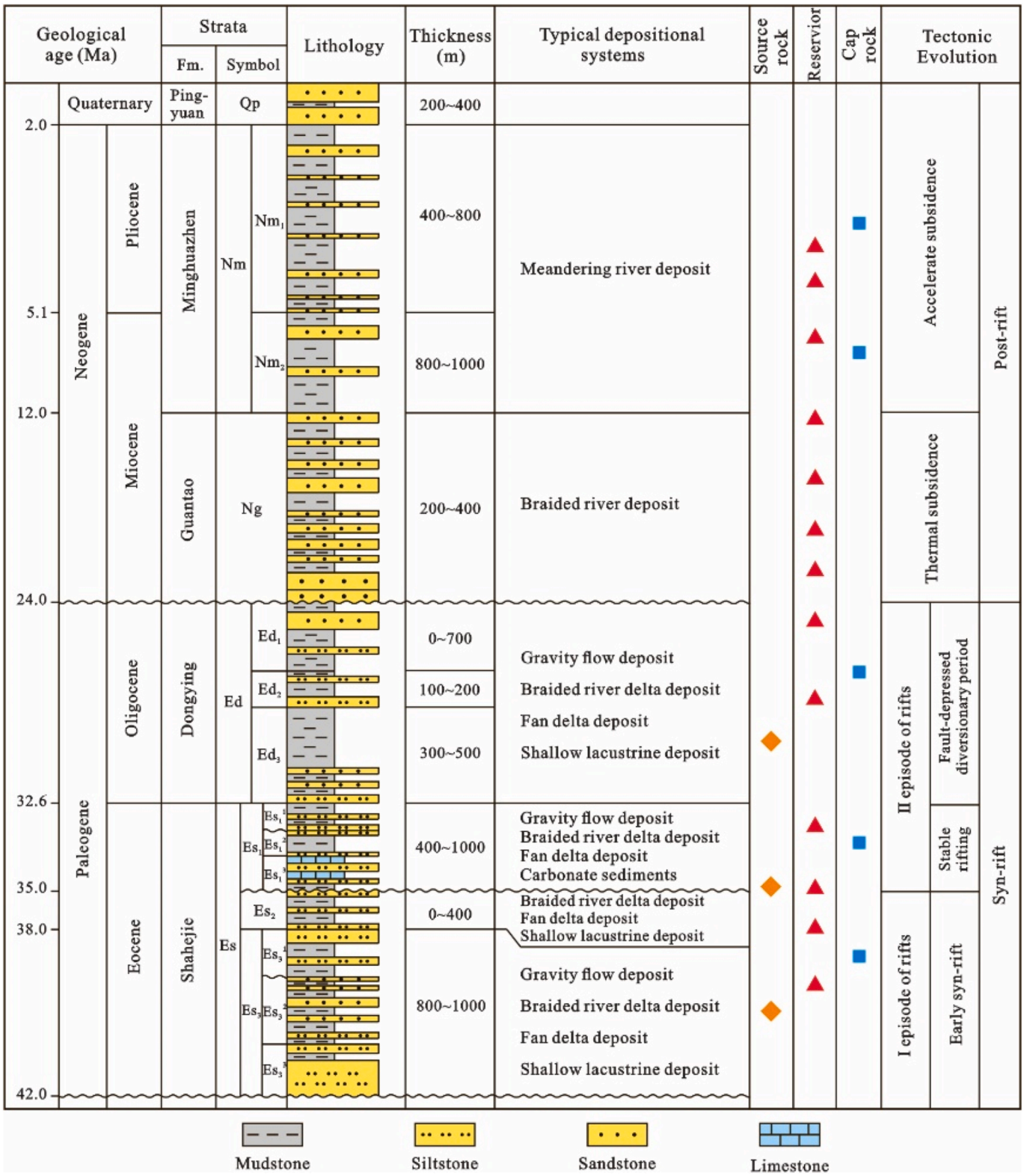

Fig. 2. Comprehensive stratigraphic column of the Qibei slope (For detailed sedimentary evolution, see Chen et al., 2014).

Multiple wells are selected to make high-precision synthetic seismic records to perform fine-layer interval calibration. It is found that the TWT shows regular change with the depth, and the relationship between them can be expressed as a second-order polynomial (R^2 is 0.999), through which the actual depth at any point in the seismic profile can be obtained (Fig. 5). The unit 'ms' in the following text represents the depth of the TWT, and the unit 'm' represents the actual depth or throw.

The test data of reservoir samples are also provided by the Exploration and Development Research Institute, Dagang Oilfield Company (Location of the sample points is shown in Fig. 1C). The homogenisation temperature of fluid inclusion analysis data was obtained from 26 sandstone samples of 12 wells (sample depths are shown in Table 1),

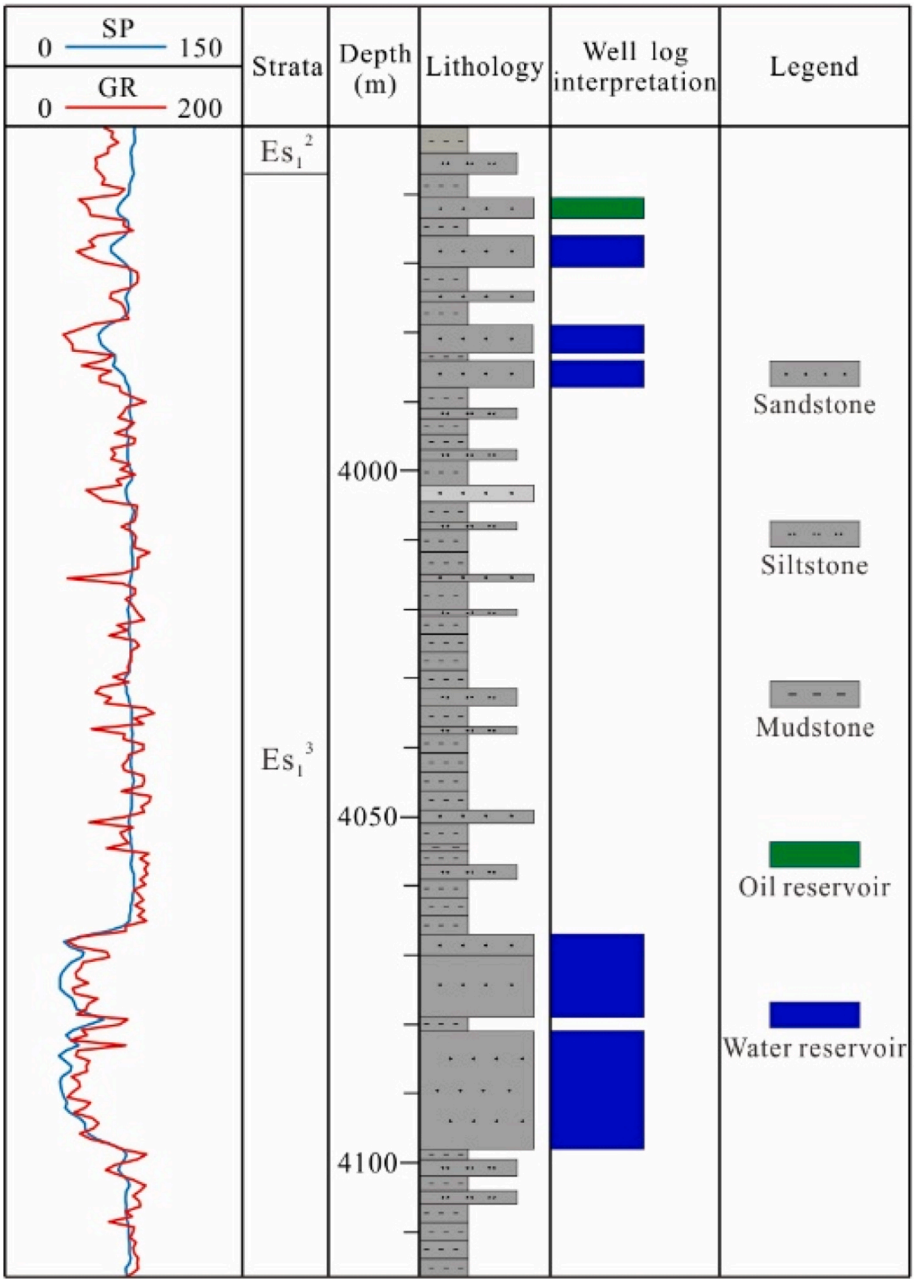

Fig. 3. Comprehensive column of well BS22. The logs, lithology and oil reservoir are shown. See Fig. 1C for well location.

combined with well burial history simulation to analyse the charging history of hydrocarbons in the study area.

4. Results

Hydrocarbons are mainly distributed near fault F1, so we especially study the characteristics of this fault. Along most planes of fault F1, the thickness difference between footwall and hangingwall varies, so does the fault throw, which varies with the depth (Fig. 6).

4.1. Throw-distance (T-x) plot

A T-x plot can describe normal faults' geometry and lateral evolution (Nicol et al., 1996; Walsh et al., 2003; Mattos et al., 2016). From shallow to deep layers, we studied the variation of throws from Horizons a to j. It can be seen from the plot that, from Horizons b to d, the throws first increase and the decrease, and this process has gone through three times (Fig. 7). There are two local minima, at line 14 and line 16. According to this feature, the plot can be divided into three parts, from left to right, the three parts are named Segment A, Segment B, and Segment C. Segment A has a maximum throw value of 1132 ms at line 9, Segment B has a maximum throw value of 195 ms at line 15, and Segment C has a maximum throw value of 205 ms at line 18. From left to right, the local minimum throw values are 125 ms (line 1), 62 ms (line 14), 55 ms (line 16) and 63 ms (line 19), respectively. There is an enormous difference in the maximum throw value between Segment A and Segment B and C, and the former is about five times that of the latter. From Horizons e to j, the throws first increase and then decrease, and this happened twice. The two local maxima are at lines 9 and 18, separated into two segments at line 16.

4.2. Throw-depth (T-z) plots

The detailed longitudinal T-z plots for each crossline are shown in

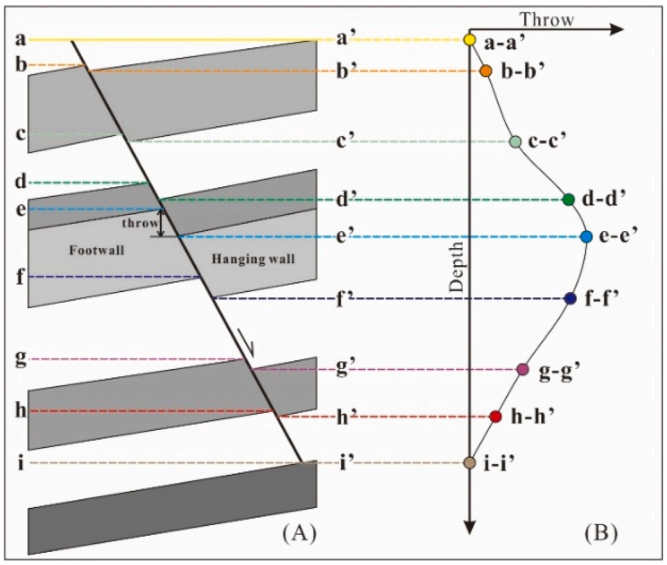

Fig. 4. The calculation of fault throws for each interval in the seismic profile (modified after Maunde and Alves, 2022). (A) Schematic diagram of calculating the fault throw with depth along a normal fault. (B) Schematic diagram of the change of fault throw with depth (T-z plot).

Fig. 8. From shallow to deep, the fault throws gradually increase. The throw values of line 1 ~ line 5, line 13, line 14, line 18 and line 19 have gone through the process of increasing-decreasing three times, while line 6, line 7, line 11, line 12 and line 15 ~ line 17 experienced two increasing-decreasing processes. Line 8 to line 10 are relatively special, and the throws continue to increase from top to bottom. In general, from 1000 ms to 2250 ms, the throw values are relatively small, and to further deeper, the values are relatively large, with the maximum values at the horizon b. From the comparison of the three segments, the fault throws of Segment A is larger than that of segment B and C. In the range of line 8 to line 10 of segment A, throw values are very large in the deep, exceeding 1000 ms, and the maximum throw value of this fault is at the horizon b of line 9, which is 1132 ms.

4.3. Throw contour map

Fig. 9 is the throw contour map of fault F1, showing the change of fault throw of different measuring points on the fault plane. The maximum fault throw generally appears near the centre of the fault plane (Childs et al., 2003; Kim and Sanderson, 2005; Lathrop et al., 2021), and the maximum fault throw appears near 3000 ms of line 9. From this position up to 2000 ms, the contours are parallel or nearly parallel, consistent with the distribution pattern of the fault contours of typical syn-sedimentary faults (Nicol et al., 1996; Childs et al., 2003; Baudon and Cartwright, 2008a). In areas with a depth greater than 1800 ms, in addition to this maximum throw, there are two relatively large throws at 3000 ms of line 15 and line 18, respectively. These three large throws are separated by throw minima areas roughly at line14 and line16, which are consistent with the lateral local minimum throw values of the T-x plot. On the left side of line 13, the throws are relatively small near the depth of 1750 ms, and the small values on the right side are distributed around 2000 ms. The depth at which these small throws are located can divide the fault plane into upper and lower segments so that the fault plane is divided into six segments. In segment A-1 and Segment C-1, there are relatively large fault throws at a depth of about

Table 1
Sandstone sampling depth table. See Fig. 1C for well locations.

Well	Well depth (m)	Sample depth (m)	Well	Well depth (m)	Sample depth (m)
BS22	4850.0	4616.5, 4617.5	GS40	4465.0	4101.6, 4193.9, 4194.3
G338-1	3459.8	2818.6, 2831.3, 2836.7	GS46	4313.4	3379.6, 3381.9, 3390.5
GS15	4038.1	3845.6	GS53	4017.9	3627.5
GS21	4424.8	3863.5, 3865.5, 3869.0	GS59	4110.0	3945.5
GS35-1	4526.0	4102.6	GS74-1	3797.0	3401.9, 3425.6, 3429.1
GS39	4216.0	3843.5, 3855.6, 3970.9	QS6	5269.0	4536.2, 4729.0

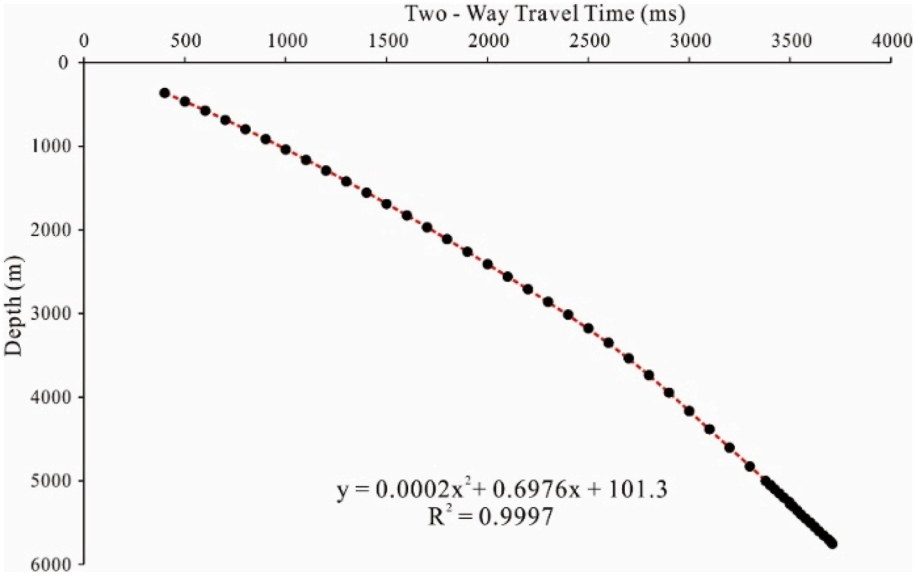

Fig. 5. TWT (ms) versus actual depth (m) plot, the red dashed line is the fitting line. The figure shows the second-order polynomial obtained by fitting and the confidence R^2 value of this polynomial. (For interpretation of the references to colour in this figure legend, the reader is referred to the Web version of this article.)

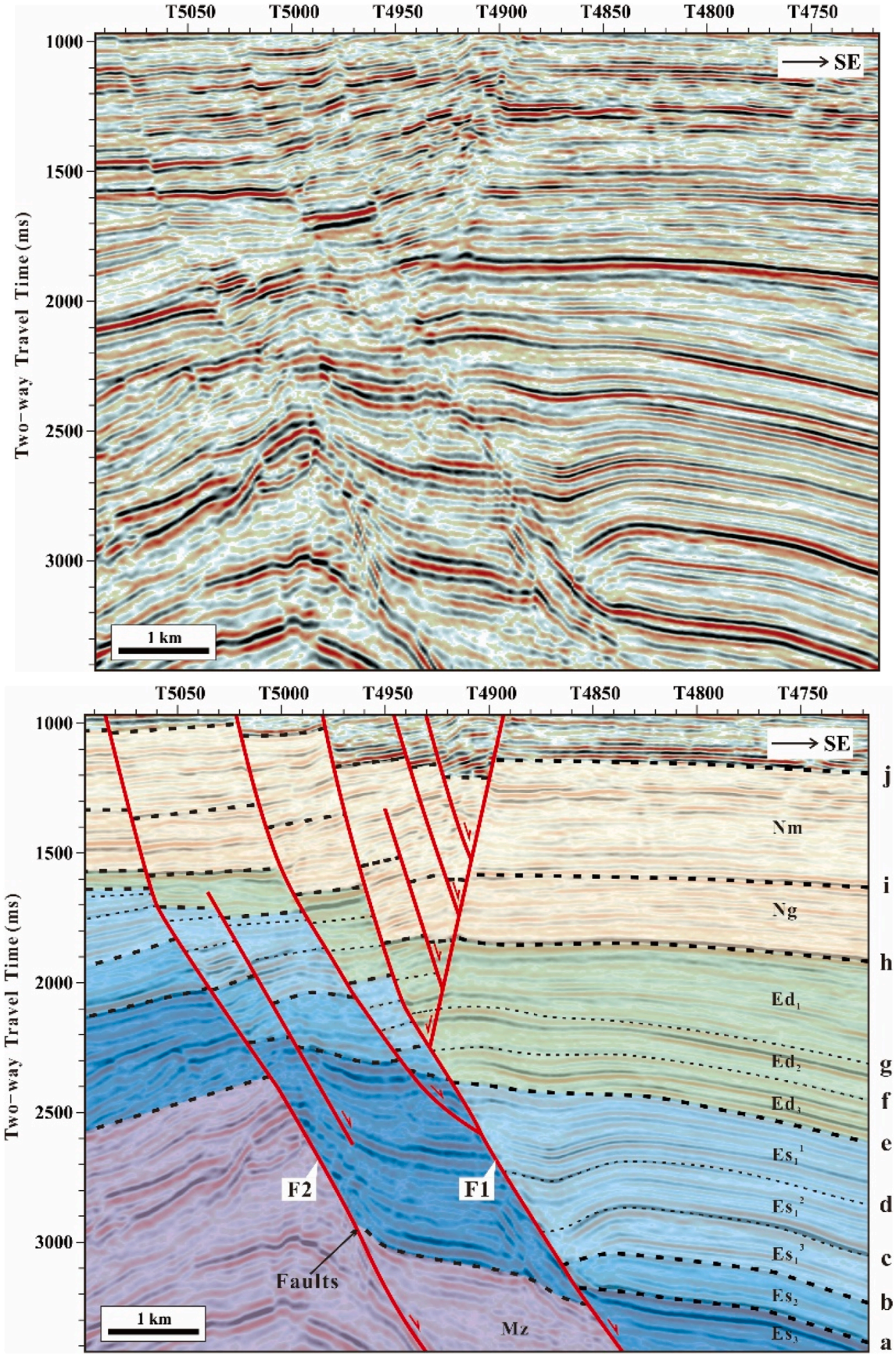

Fig. 6. Uninterpreted (above) and interpreted (below) seismic profiles, the latter showing the interpreted stratigraphic intervals and faults (Line 3 in Fig. 1C). Horizon a to j on the right side of the interpreted one are the codes of the dividing lines of the intervals (for standard seismic interpretation, see Misra and Mukherjee, 2018).

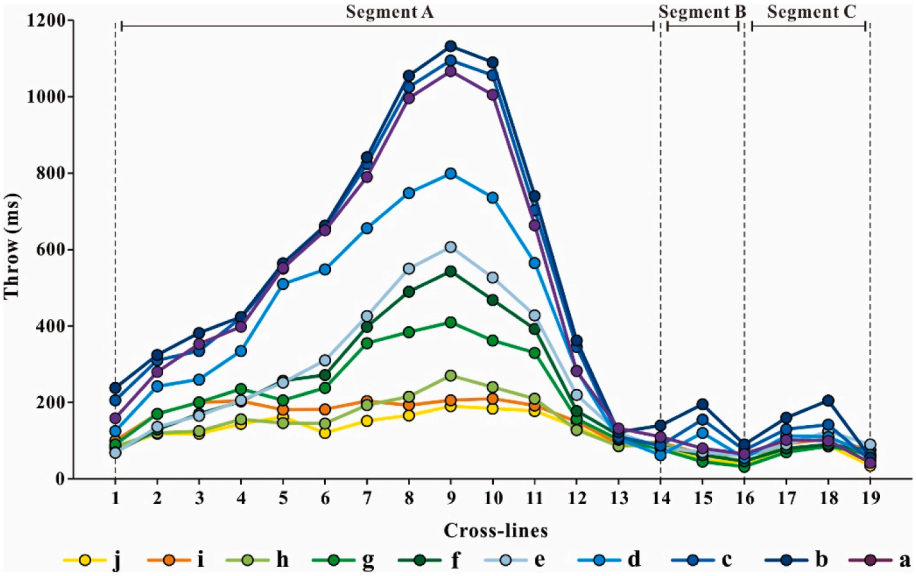

Fig. 7. Throw-distance (T-x) plot of fault F1. According to the change of the throw, it can be divided into three segments, namely Segment A, Segment B and Segment C. The maximum throw values of Segment A, B and C are different. The ordinate is presented as TWT, and the abscissa is the serial number of the equally-spaced seismic profiles.

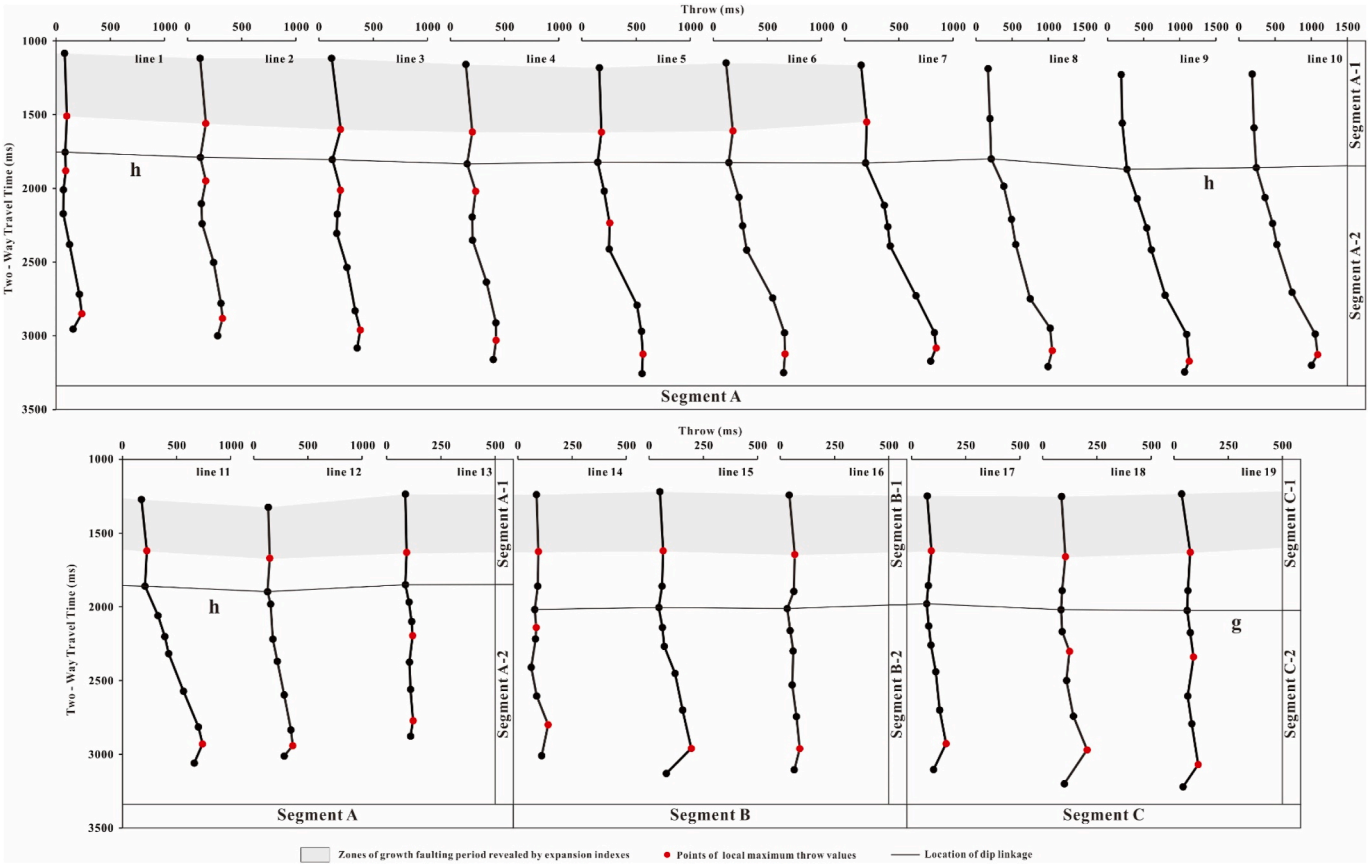

Fig. 8. Fault throws versus depth (T–Z) plots at 19 equidistance measuring points of fault F1. Due to the significant difference in the maximum throw values between different crosslines, and to better show the variation of the throws with depth, the maximum value of the abscissa varies between 500–1500 ms (TWT).

1500 ms, which may mean that the fault also has centres in the shallow layer.

4.4. Expansion index (EI) plots

Fig. 10 displays the EI of different crosslines of the fault F1. In Segment A, from line 1–7 and line 11–13, the fault went through multiple periods of activity, and the last period of inactivity is the deposition

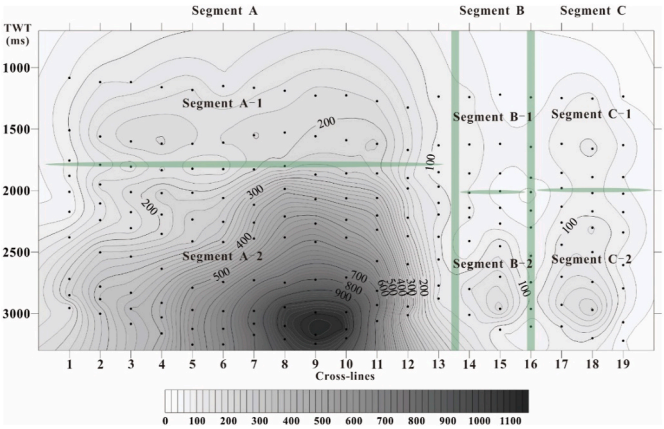

Fig. 9. Throw contour map of fault F1. One hundred ninety throw values were measured. TWT: two-way travel time. Dark colour represents a greater throw value, with a maximum of 1132 ms and a minimum of 32 ms. (For interpretation of the references to colour in this figure legend, the reader is referred to the Web version of this article.)

period of Ed_1. Line 8 to line 10 of Segment A are different from other crosslines, and the fault continues to be active during the geological history. Notably, from line 5 to line 10, when the depth is around 2700 ms, the EI values are tremendous, indicating that the fault was highly active at that period of geological history, with a large set of sediments deposited on the hangingwall. In Segment B and C, the fault is multi-period activities. Although the fault in these areas was also inactive during the deposition of Ed_1, unlike Segment A, the fault has been inactive since the deposition of Ed_2. Except for line 8 to line 10, the EI value is less than or equal to 1.0 near the Ed_1, speculating that the fault was inactive during this geological time. In the range from 1100 to 1700 ms above the Ed_1, the EI value is greater than 1.0, indicating that the fault was reactive. In this area, the thickening of the strata on the hangingwall of the fault F1 can also be observed on the seismic profile, indicating that syn-sedimentation occurred after the deposition of the Ed (Fig. 6).

4.5. Determination of the charging time

Homogenisation temperature of aqueous inclusions with the similar microscopic characteristics to hydrocarbon inclusions are distinct in the samples from different formations. The Ed samples at a depth of 2818.6–2836.7 m show one period of homogenisation temperature. The homogenisation temperature of brine inclusions ranges from 80 °C to 120 °C, concentrating around 90–110 °C (Fig. 11A). The Es_1^3 samples at a depth of 3843.5–4194.3 m, have homogenisation temperatures ranging from 80 °C to 160 °C, concentrating around 120–140 °C (Fig. 11B). As for the sandstones in the Es_2, samples from Well BS22, with depth at 4616.5 m and 4617.5 m, also show one period of homogenisation temperature, ranging from 120 °C to 170 °C, concentrating around 130–150 °C (Fig. 11C). The samples of the Es_3 are from Well QS6, with depth from 4536.2 m to 4729.0 m, has only one period of homogenisation temperature, ranging from 100 °C to 170 °C, concentrating around 130–150 °C (Fig. 11D).

Due to the lower compressibility of fluids in the aqueous inclusions, the homogenisation temperatures are closer to the trapping temperatures, so the accurate capture temperature can be obtained by measuring the aqueous inclusions (Volk and George, 2019). We use the thermal and burial history simulation combined with homogenisation temperature values of aqueous inclusions to judge the hydrocarbons charging history of the Ed and Es traps. We choose well QS6 to study the charging history of hydrocarbons in the reservoirs of the study area (Fig. 12). The hydrocarbons in the Es_3 reservoirs were mainly charged from 31.1 Ma to 27.5 Ma. Ed, Es_1^3 and Es_2 reservoirs have similar hydrocarbon charging times, with an accumulation of medium-maturity oils in the reservoirs from 3.9 Ma to 0.3 Ma. Judging from the homogenisation temperature projected onto the burial history simulation, the Ed and Es reservoirs in the study area have experienced two periods of hydrocarbon charging stages. Hydrocarbons in the reservoirs from the Es_2 to the Ed were mainly captured during the second stage. The first stage occurred during the deposition of the Ed (late Paleogene), and the second stage occurred from the deposition of the Nm to the present (late Neocene to Quaternary).

5. Discussion

5.1. Evolution processes of the fault

We have studied the characteristics of the fault throws in different areas of fault F1 in detail because oil and gas are mainly distributed around this fault nowadays (Fig. 1C). In order to analyse its control effect on hydrocarbon distribution, further analysis of the fault evolution is needed.

5.1.1. Lateral linkage of the segment faults

There are three large throw values in the regions A-2, B-2 and C-2 near the depth of 3000 ms on the throw contour map (Fig. 9). Generally speaking, the relatively large throw in the contour map represents the centre of the fault plane, so it can be considered that there may be three isolated faults during the early stage of the fault evolution. However, the fault F1 currently has only one fault plane, so the fault should have undergone a process of lateral linkage during the evolutionary process.

In addition to the fact that there is only one fault plane, which can indicate that the fault has experienced the process from isolation to interaction, the T-x plot can also reflect the lateral evolutionary stage of the fault to a certain extent (Kim et al., 2001; Walsh et al., 2003; Jackson and Rotevatn, 2013). When the fault is in the early stage of isolated faults, each fault has an independent fault plane reflected in the T-x plot as several independent faults throws change with distance (Fig. 13, Stage 1). As the faults continue to evolve, the faults expand laterally and propagate toward each other. At this time, each fault still has an independent fault plane, but the faults overlap (no linkage) in the direction perpendicular to the fault strike, which is reflected in the T-x plot as several isolated curves with intersections (Fig. 13, Stage 2). In the ultimate stage of fault evolution, the hard linkage stage, several isolated faults are linked to form a new fault plane, which is reflected in the T-x plot as a curve of fault throws changing with distance (Fig. 13, Stage 3). The curves from Horizon b to Horizon d in the T-x plot of fault F1 have similar characteristics to the plot curve of the hard-linked segment faults stage, which means that the fault should have been hard-linked.

Regions A-1 and C-1 of the contour map also has relatively large fault throw points at the depth of 1500 ms, which may reflect that there are some faults in the shallow layer that evolve independently and then hard-linked with other faults (Fig. 9). The characteristics of the curves from Horizon h to Horizon j in the T-x plot (Fig. 7) are also similar to those of the plot in the hard-linked segment faults stage, indicating that hard-linked faults should have also occurred in the shallow layer.

5.1.2. Dip linkage of the fault

In addition to the interaction of the faults in the lateral direction, there are also linkages in the longitudinal direction. To simplify the description, we use a “cone-shaped” (C-type) pattern to describe the T-z plot (Fig. 14). This pattern is an almost symmetrical curve with a relatively uniform change in fault throw with depth, that is, the slope does not change significantly, and has a maximum throw in the centre (Muraoka and Kamata, 1983).

In the T-z plot (Fig. 8), from line 1 to line 6 of Segment A, the Horizon h are local minimum throws, and the throws below and above it are all C-type profiles, with low throw values at the upper part of the fault, which is similar to the T-z plot of a typically isolated fault (Jackson and

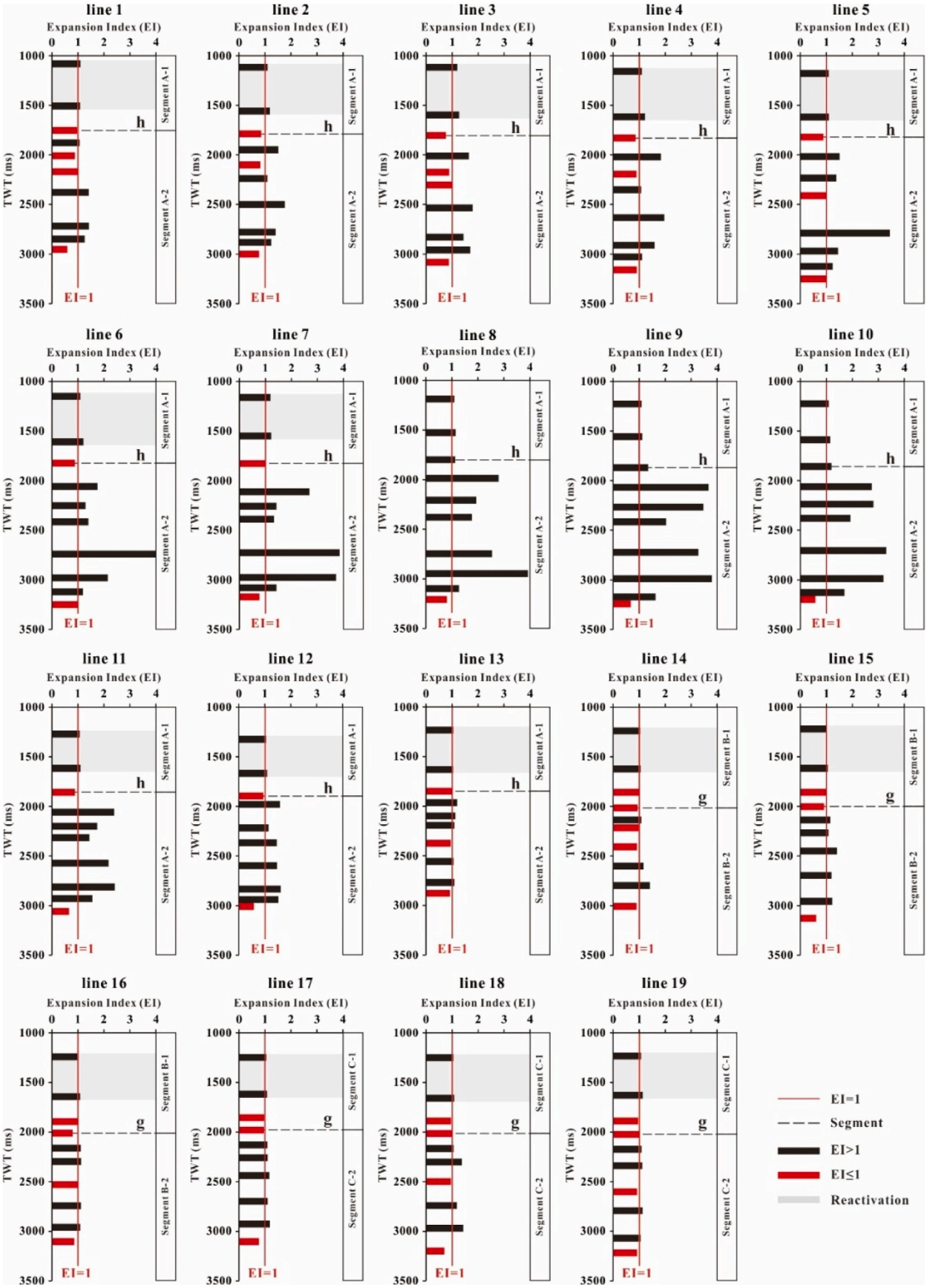

Fig. 10. Expansion index (EI) plots of the 19 equally spaced seismic profiles of fault F1. An EI value greater than 1.0 indicates a significant increase in the thickness of the fault hangingwall, while an EI less than 1.0 indicates a decrease in the thickness of the fault hangingwall. The grey shaded area represents the reactivity of the fault above the Ed. TWT: two-way travel time.

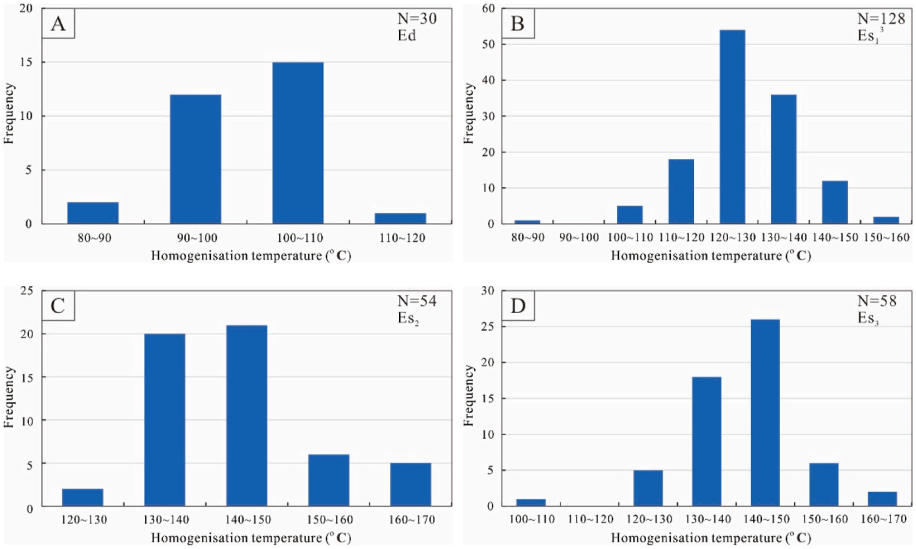

Fig. 11. Homogenisation temperature distributions of aqueous inclusions in reservoir samples. (A) Ed, (B) Es_1^3, (C) Es_2, (D) Es_3.

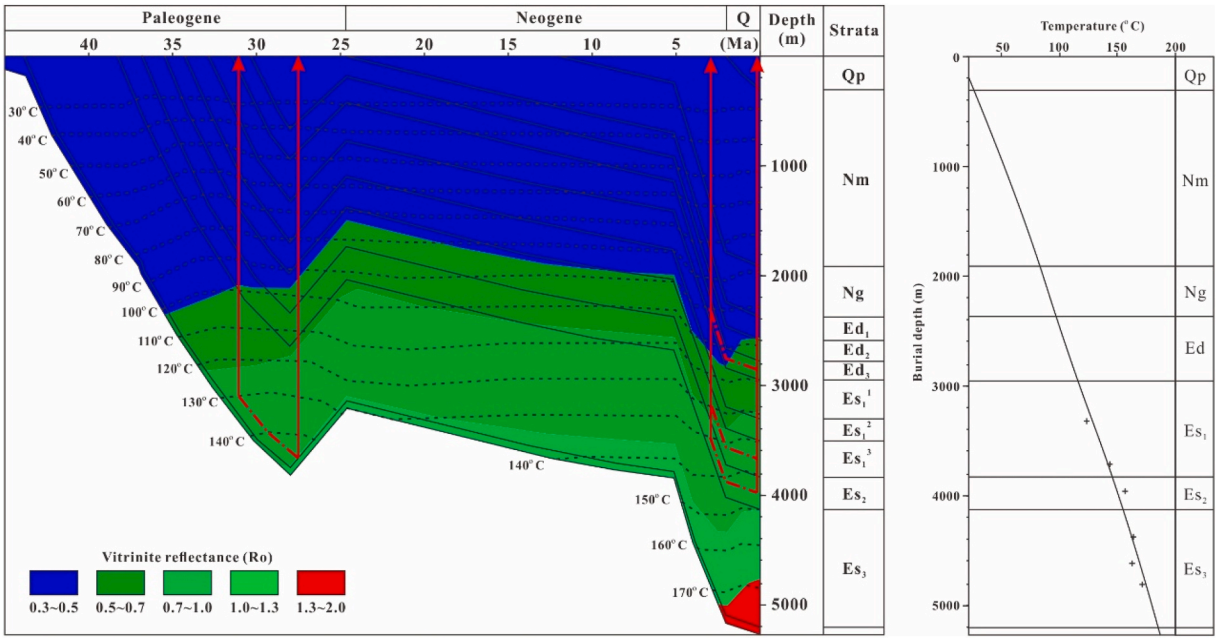

Fig. 12. Thermal and burial history of Well QS6, showing the two charging stages. See Fig. 1C for well location.

Rotevatn, 2013). Segment B and C have similar characteristics to the western part of Segment A, except that the local minimum is on the Horizon g. In the upper part of the fault, the maximum throws are between 1500 ms and 1700 ms, and in the lower part, the maximum throw is around 3000 ms. The maximum value of the fault throws generally represents the normal fault's nucleation sites, indicating that there should be centres on both upper and lower sides (Fossen, 2020). Therefore, we speculate that the upper and lower faults are two isolated faults, which influence each other during the evolution of the faults and eventually hard-linked and then evolve into a complete fault plane.

For the lower part of the fault, line 1 to line 7 and line 11 to line 19, it may have a free surface at first and then evolve into a blind fault: (1) the throw curve of the T-z plot is C-type (Fig. 8); (2) the EI value of the Horizon h is less than 1.0 (Fig. 10). However, for another part of the area, line 8 to line 10, the throw from the maximum to Horizon h decreases rapidly, which may indicate that the fault has encountered a confined layer due to the existence of a free surface (Fig. 8; Childs et al., 2003; Baudon and Cartwright, 2008a; Jackson and Rotevatn, 2013; Cong et al., 2020). The evolution of fault in this area is just the opposite of the areas discussed earlier. The fault evolves as a blind fault and then breach the free surface upwards as a growth fault, accompanied by a significant increase in the thickness of the hangingwall that can be observed on the seismic profile (Fig. 6) and the EI values greater than 1.0 (Fig. 10; Baudon and Cartwright, 2008b; Cong et al., 2020).

However, when the upper and lower faults are linked, what state the fault is in (active or inactive) still needs to be answered. We cannot get an accurate linkage time between the upper and lower faults, but the approximate time range can be inferred. From the T-z plot, the minimum fault throw is at Horizon h (line 1 to line 7 and line 11 to line 13) and horizon g (line 14 to line 19), so it is speculated that the upper and lower faults were connected roughly during the Ng deposition period. During this period, the fault was in an active state (Fig. 10). At the same time, the value of the fault throw was greater than zero and was not the minimum value of all measuring points in a profile, and the geometry of

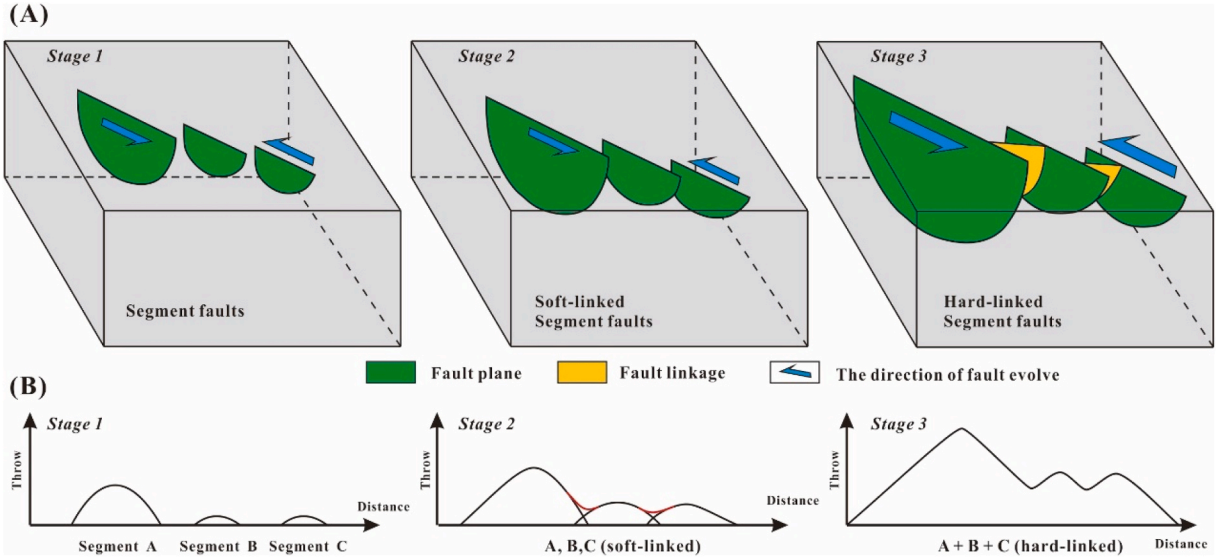

Fig. 13. Schematic diagram of fault lateral evolution, showing the process of faults from isolation to interaction (modified after Kim and Sanderson, 2005). (A) Three-dimensional schematic diagram. (B) Variation of throws with distance.

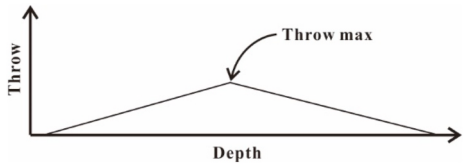

Fig. 14. Idealised T-z plot of a C-type fault (modified after Muraoka and Kamata, 1983).

the upper and lower faults was similar (Fig. 8), so we speculated that the two parts of the fault should be active when they were dip linkage (Cong et al., 2020).

Based on previous analysis, we believe that the evolution of faults can be divided into four stages: (1) Three isolated faults were formed at the beginning, including one large fault and two small faults. The three faults experienced the isolated faults stage, soft-linked stage and hard-linked stage, and finally formed a fault (Fig. 15A). (2) There were regional differences in fault evolution at this stage. The area from line 8 to line 10 continued to be active and did not become a blind fault, while the fault activity gradually decreased and became a blind fault in the other areas (Fig. 15B). (3) With the continuous deposition of stratum, two isolated blind faults were formed in the upper stratum on the left and right of fault F1 (Fig. 15C). The area from line 8 to line 10 was still active, but the activity during this period was significantly reduced. (4) The isolated faults on the left and right sides were linked with the lower part, and finally, fault F1 was formed (Fig. 15D).

5.2. Fault-caprock coupling controlling hydrocarbon enrichment

The clastic stratum in the Qibei slope is mainly dominated by braided river delta, fan delta, gravity flow and shallow lacustrine deposits (Fig. 2; Pu et al., 2014; Zhao et al., 2017). Due to the development of overpressure and fractures, the physical properties of Paleogene reservoirs have been improved, making them suitable and promising hydrocarbon reservoirs (Pu et al., 2013). There are multiple layers of source rocks (Es_3, Es_1^3 and Ed_3) in the study area, some of which have reached the oil window and can generate hydrocarbons (Fig. 12; Wang et al., 2014; Zhang et al., 2019). Multiple faults can be found in the strata on the seismic profile (Fig. 6). These faults, high-quality reservoirs and the widely distributed caprocks in the region have formed many fault-controlled traps from the deposition period of the Ed to the early

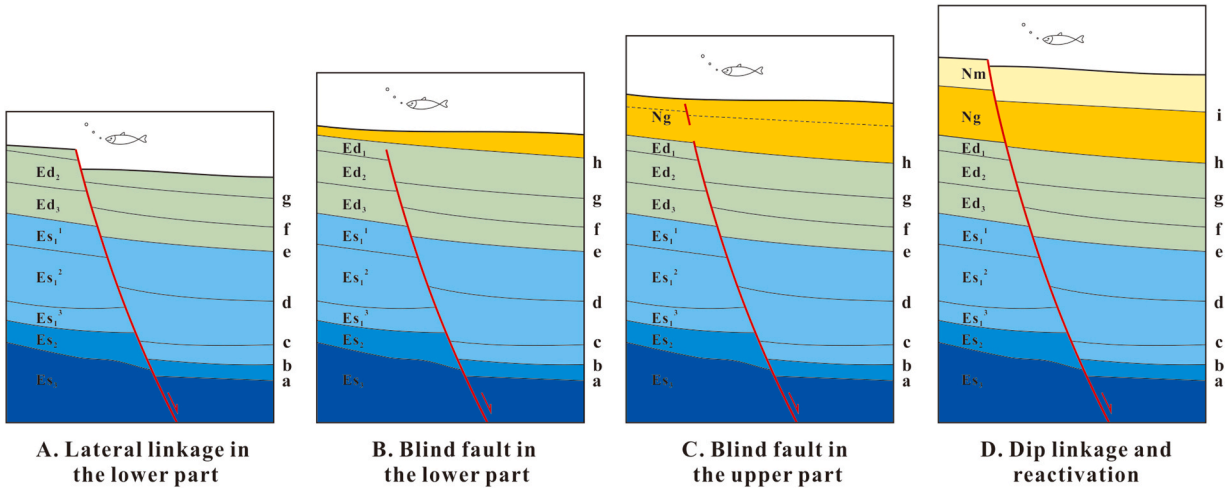

Fig. 15. Schematic evolutionary model of fault F1, which experienced four stages.

deposition stage of the Nm. The existence of fault-controlled traps and source rocks reaching the oil window indicates whether the Paleogene traps in the study area can accumulate hydrocarbons are determined by the hydrocarbon transport capacity of faults and whether the hydrocarbons can ultimately be preserved is determined by the sealing capacity of the caprock.

5.2.1. Hydrocarbon distribution and factors controlling the distribution

The hydrocarbons are dispersed in multi-layered reservoirs in the study area, and the longitudinal distribution varies greatly (Fig. 2). Exploration discoveries have been made from the Nm at a depth of about 1000 m to the Es_3 at a depth of 5000 m. The fault-block traps in the shallow Nm of Gangdong Oilfield have been exploited for more than 50 years, and there are also a few fault-block traps in the Ng. In addition to the fault-block traps in the deep layer, the fault-controlled reverse drag anticlinal traps are discovered in the Maxi and Madong oil fields (Hu et al., 2019). According to the current exploration, a large amount of Paleogene hydrocarbon reservoirs were found on the hangingwall of the fault F1 (Fig. 1C; Zhou et al., 2019).

The entire study area can be divided into three segments through the T-x plot (Fig. 7) and throw contour map (Fig. 9). The number of faults linking the source rocks and the traps is different in the three segments, which also affects the special distribution of hydrocarbons. The distribution of hydrocarbons in Segment A is mainly controlled by fault F1. In addition to the influence of fault F1, Segment B and Segment C are also controlled by multiple near-parallel faults (Fig. 1C). Apart from the effect of the number of faults, the throw values of fault F1 at different study area locations are different, affecting the stratum structure, forming two types of traps, reverse drag anticlinal trap and fault-block trap.

Fault F1 links the mature source rocks to multiple traps in Segment A. Although the fault links numerous traps, in the area of line 1 ~ line 3 in the west of Segment A, oil reservoirs are only found in the Es_1^3 fault-block traps (Fig. 16). Judging from the seismic profile, the integrity of the caprock in this area has not been damaged, which may have prevented hydrocarbons from migrating to the shallow layer, resulting in no oil layer being found when there are traps in the shallow layer. In the central and eastern part of Segment A, line 4 ~ line 12, in addition to hydrocarbons found in the Es and Ed, oil reservoirs were also found in the Nm and Ng fault-block traps, which is different from the distribution of oil reservoirs in the west (Fig. 17). This may be affected by the large fault throw, where the maximum throw value is greater than 1000 ms, and there are large throws in the area from line 5 to line 11. During the deposition period of the Es and Ed, the thick column of sedimentary was filled on the hangingwall of the fault. Under the control of differential compaction, gentle bending folds are formed on the hangingwall, that is, the reverse drag anticlinal traps (Nabavi and Fossen, 2021). From the Es_2 to the Ed, reverse anticlinal drag traps gradually become smaller to disappear completely. During the second charging stage, the reactivation of fault F1 formed a good matching relationship with the previously developed traps, resulting in the accumulation of hydrocarbons under the regional caprock. Affected by the large fault throw, the continuity of the regional caprocks was destroyed, and the caprocks on both walls of the fault are no longer juxtaposed. Therefore, hydrocarbons can migrate across the caprocks to the shallow layer and accumulate in the upper traps, where Nm and Ng traps are affected by mudstone layers.

Segment B and Segment C are generally similar but different from Segment A. In Segment B and C, a series of small-throw faults are formed on the hangingwall of fault F1, with a similar strike and nearly parallel to fault F1. These faults link source rocks and traps, and large area oil reservoirs have been discovered in Es_1^3 fault-block traps under the Es_2 caprock (Fig. 18). In addition to these oil reservoirs, oil reservoirs have also been found in the Ed and above. From the seismic profile, the intact of the Es_1^2 and Ed_2 caprocks has not been destroyed, which should be the reason why hydrocarbons are preserved in the Es_1^3.

From the previous analysis, although the study area is fault-block reservoirs, their longitudinal distribution is different. They all have oil reservoirs in the Es_1^3 while Segment A and C have also discovered oil reservoirs in shallow layers (Figs. 17 and 18). In the second charge stage, the fault has completed dip linkage, forming a vertical migration pathway. Although the fault throw is not so large relative to the deep layer (Fig. 8), the EI values are all greater than 1.0 (Fig. 10), indicating that the fault is active and hydrocarbons have the ability to transport upward along the fault. However, the difference in distribution indicates that hydrocarbons cannot migrate upward along the entire fault plane, which may be related to the thickness and integrity of the caprock.

There are two regional caprocks in the study area, and whether there are oil reservoirs above these two regional caprocks is an important criterion for judging whether the caprocks are effective. The oil layer distribution of each well in the study area is statistically divided into three types according to whether oil layers are found above the caprock. Type I, oil reservoirs are found above and below the Ed_2 caprock; type II, oil reservoirs are found above and below the Es_1^2 caprock, but there is no oil layer above the Ed_2 caprock; type III, oil reservoirs are only found below the Es_1^2 caprock. According to the previous analysis, there is a difference in whether the continuity of the Es_1^2 caprock is destroyed in the study area. From line 4 to line 11, the continuity of the Es_1^2 caprock is destroyed, and hydrocarbons are found in the reverse drag anticlinal traps. Faults only partially destroy the continuity of the caprock in the other areas, the caprocks on both walls of the fault are still juxtaposed, and oil reservoirs are found in the fault-block traps. Therefore, type III is subdivided into two types, type III_1 represents the latter, and type III_2 represents the former. Classification results are shown in Table 2.

Type III_2 hydrocarbons accumulate in the reverse drag anticlinal traps, and their accumulation is mainly determined by the area and amplitude of the reverse drag anticlines. The other three types are all fault-block traps and are jointly affected by faults and caprocks. We focus on these three types of control factors for accumulation.

5.2.2. Effective thickness of caprock

When evaluating the argillaceous caprock sealing ability, the critical evaluation parameter at the much smaller scale is the displacement pressure of the caprock, which can also be expressed by hydrocarbon column height that can be capped (Jin et al., 2014). Macroscopically, it is to study the thickness and distribution of the caprock (Ma et al., 2019). A thicker caprock is less susceptible to faults and can ensure continuity and intact, and larger displacement pressures can seal higher hydrocarbon columns. The combination of the two aspects can prevent hydrocarbon from migrating to shallow layers. However, there is a relationship between the thickness of the caprock and the sealing capacity because the increase in the thickness of the caprock will inevitably reduce the probability of communication between the large pores, increase the displacement pressure of the caprock and increase the sealing capacity (Bai et al., 2014; Ma et al., 2019).

Ed_2 and Es_1^2 argillaceous caprocks is a known effective barrier for Paleogene reservoirs in the Qibei slope with stable regional distribution and large thickness (Zhou et al., 2019). Obtained from drilling and seismic data, the Es_1^2 caprock is distributed in the whole study area, and the depth is in the range of about 2400 ms–2700 ms. The maximum thickness of the mudstone can reach 360.0 m, 221.0 m on average, and the thickness in most of the study area exceeds 140 m (Table 2). The regional stable Es_1^2 mudstone makes the lower reservoir generally develop under-compacted zones, effectively protecting the reservoir space (Yu et al., 2010; Guo et al., 2016). In addition to the characteristics of enormous thickness and continuous regional distribution, the mudstone in the Es_1^2 also has the features of high displacement pressure. In most study areas, the displacement pressure is greater than 6 MPa. In some areas, it can reach a displacement pressure of 9 MPa or more, making the regional caprocks capable of sealing hydrocarbons (Table 3; Fu et al., 2012). The Ed_2 caprock is also steadily distributed in the whole

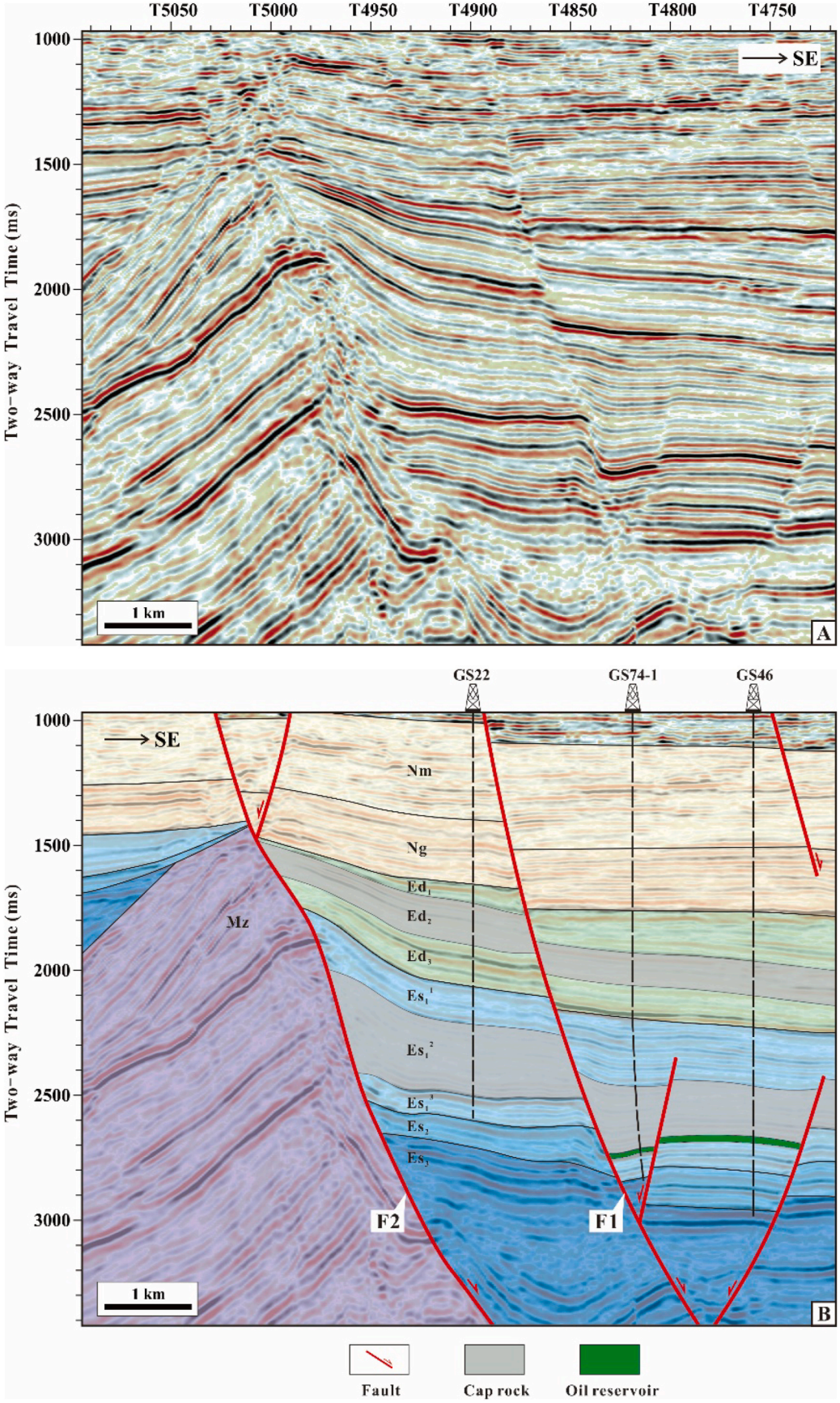

Fig. 16. Uninterpreted (A) and interpreted (B) seismic profile of line 1. The interpreted profile shows that the west part of Segment A is controlled by fault F1 and F2. Drilling shows that no hydrocarbons have been discovered on the footwall of fault F1, and the distribution of thick Ed_2 and Es_1^2 caprock on the hangingwall can prevent the hydrocarbons in Paleogene reservoirs from migrating along faults to the shallow Neogene reservoirs. See Fig. 1C for seismic profile location.

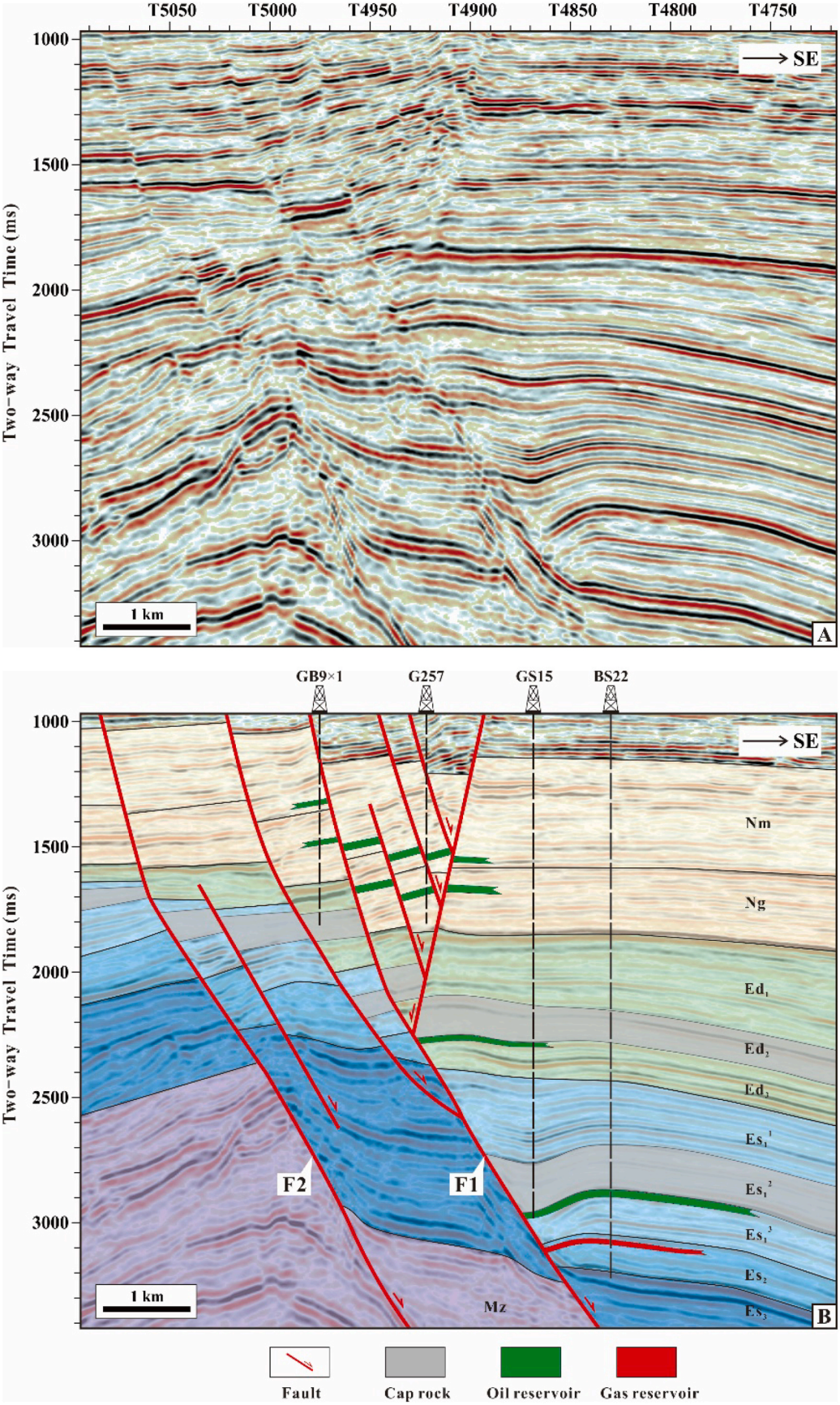

Fig. 17. Uninterpreted (A) and interpreted (B) seismic profile of line 7. The interpreted profile shows that the east part of Segment A is controlled by fault F1. Drilling shows that hydrocarbons have been discovered in multiple reservoirs vertically, reflecting that the large throw will make the caprock ineffective, allowing hydrocarbons to migrate to the shallow reservoirs. Es and Ed Reservoirs are dominated by Es_1^2 and Ed_2 regional caprocks, and shallow Nm and Ng reservoirs are dominated by mudstone layers, which are not shown in the figure. See Fig. 1C for seismic profile location.

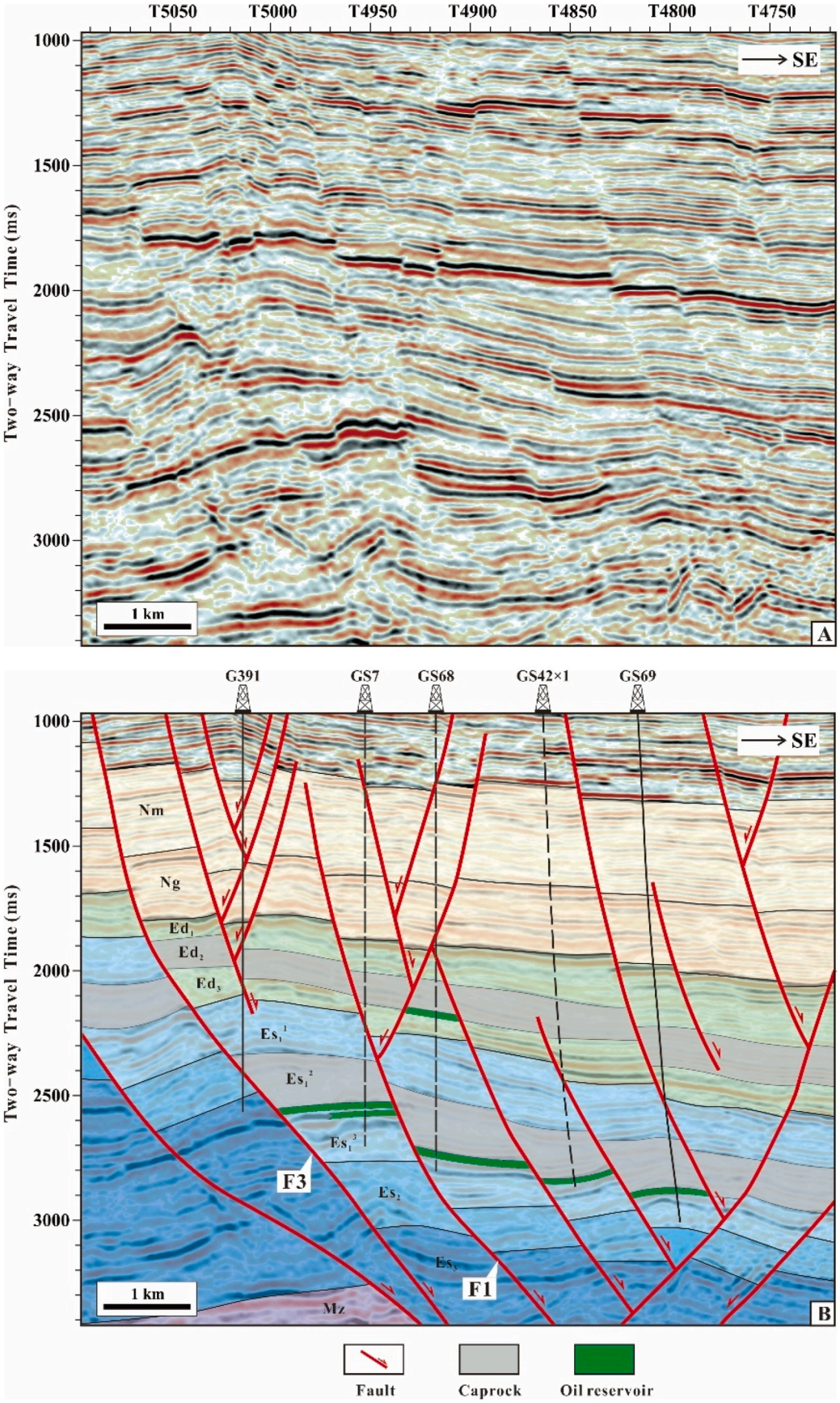

Fig. 18. Uninterpreted (A) and interpreted (B) seismic profile of line 17. The interpreted profile shows that Segments B and C are controlled by a series of faults that are nearly parallel to fault F1 in addition to fault F1 and F3. Drilling shows that hydrocarbons are widely distributed in multiple fault-controlled traps under the caprock, and the thick caprock also prevents hydrocarbons from migrating to shallow reservoirs. See Fig. 1C for seismic profile location.

Table 2
The stratum and caprock thickness statistics table of the Es_1^2 and Ed_2, statistics the strata thickness, the caprock thickness and the effective caprock thickness. The caprock thickness is based on the logging data. See Fig. 1C for well locations.

Type	Wells	Thickness of the Es_1^2 (m)			Thickness of the Ed_2 (m)		
		Strata	Caprock	Effective	Strata	Caprock	Effective
I	GS12	91.5	76.5	14.0	269.5	254.0	79.8
	GS28	346.0	312.0	108.9	426.0	402.0	109.5
	GS59	246.0	245.0	41.9	314.0	305.0	12.5
	GS66	47.5	45.5	2.4	244.0	205.0	48.3
	GX57	453.0	277.0	123.5	211.0	187.0	30.3
	QS1	175.0	143.0	125.0	278.0	207.5	97.5
	QS6	215.0	209.0	95.5	216.5	108.5	59.9
II	B102 × 1	253.0	252.0	57.8	240.0	240.0	129.4
	B109 × 1	322.9	275.5	10.8	290.0	267.5	144.8
	GS7	182.0	182.0	63.0	280.5	270.5	126.8
	GS7-2	186.0	159.5	40.5	247.0	245.0	101.3
	GS10	181.5	176.5	36.9	240.5	230.5	163.5
	GS11	165.5	162.5	69.9	233.0	213.5	143.8
	GS24-28	214.5	189.0	110.4	352.5	246.5	154.0
	GS34	304.0	304.0	122.6	281.0	270.0	126.3
	GS52 × 1	244.0	235.5	122.4	289.0	257.0	187.2
	GS64	214.5	214.5	126.0	239.0	201.0	133.6
	GS67	38.0	38.0	20.0	297.0	226.0	173.5
	GS68	213.0	209.0	14.8	211.0	193.0	82.4
	GS68 × 1	239.0	239.0	125.5	239.0	218.5	176.6
	GS69	215.5	211.5	123.0	231.0	200.0	132.6
	GS75	325.0	300.5	115.4	207.0	202.0	131.8
III_1	B108 × 1	302.0	257.5	172.9	300.5	261.0	/
	BS13 × 1	354.0	353.0	205.5	212.0	192.0	/
	GS42 × 1	190.5	190.5	130.1	216.5	204.5	/
	GS46	267.5	195.0	169.9	200.5	195.0	/
	GS58-1	354.0	271.5	128.3	278.0	235.0	/
	GS63-2	177.0	169.5	151.5	308.0	256.5	/
	GS69 × 1	385.0	360.0	275.4	187.5	171.0	/
	GS74-1	236.0	172.0	146.9	288.5	283.0	/
	GS78	325.0	242.0	130.6	264.0	192.5	/
	GS79	158.0	158.0	129.7	226.0	203.5	/
III_2	BS22	222.0	193.5	/	344.5	314.5	/
	GS13	226.5	217.0	/	362.0	350.5	/
	GS14	242.5	240.0	/	234.0	234.0	/
	GS15	377.5	343.0	/	218.5	201.0	/
	GS16	267.0	165.5	/	272.0	260.5	/
	GS19	223.0	223.0	/	249.0	223.5	/
	GS21	234.0	230.0	/	222.0	222.0	/
	GS30	230.5	192.0	/	336.0	302.0	/
	GS35-1	362.5	293.0	/	351.5	312.0	/
	GS39	298.0	261.0	/	213.5	187.5	/
	GS40	453.5	322.5	/	192.0	172.5	/
	GS53	264.0	264.0	/	314.5	305.0	/
	GS72	263.0	243.0	/	346.5	318.0	/

Table 3
Displacement pressure of caprock in the study area (from Fu et al., 2012). In the article of Fu et al., after correction, it was the displacement pressure when the mudstone was saturated with water. See Fig. 1C for well locations.

Well	Strata	Depth (m)	Lithology	Measured displacement pressure (MPa)	Corrected displacement pressure (MPa)
G339	Ed_2	2700.8	Mudstone	1.43	2.3
GS66	Es_1^2	3441.5	Mudstone	3.81	5.3
GX57	Es_1^2	3477.1	Mudstone	6.68	9.2
GS19	Es_1^2	3521.2	Mudstone	4.76	6.5
GS18-1	Es_1^3	3272.6	Mudstone	2.93	4.2
GS67	Es_1^3	3846.1	Mudstone	1.14	1.5

area, at a depth of 1800 ms–2300 ms, with a maximum thickness of 402 m, a minimum thickness of 108 m and an average thickness of over 238 m (Table 2). Only the sample from Well G339 tested the displacement pressure of the Ed_2 mudstone, and the corrected displacement pressure is 2.3 MPa (Table 3; Fu et al., 2012). Since there is only one test data, the displacement pressure value of this layer is only used as a reference.

There are differences in the longitudinal distribution of the oil reservoirs in the study area, which may be controlled by the regional caprock and the fault throws, so we try to find the lower limit of the thickness of the caprock that controls the reservoir distribution.

The main charging stage in the study area is the deposition period of the Nm (Fig. 12). During this period, the fault is active (Fig. 10). Therefore, the magnitude of the fault throws may affect whether the hydrocarbon can migrate along the fault connecting the source rock. Taking the fault throws during the deposition period of Nm as the abscissa and the thickness of the caprock as the ordinate, a scatter plot of the caprock versus fault throw is established (Fig. 19). Judging from the scatter plot, it seems that there is no lower limit for the thickness of the caprock, which can effectively determine whether there is an oil reservoir above the caprock. However, there seems to be a lower limit of the fault throw, and no oil reservoirs are found in traps smaller than this fault throw.

The scatter plot does not show an obvious lower limit of the thickness, which may be affected by the damage of the caprock continuity by faults. Although the thickness of the caprock in the study area is large, the continuity of some caprocks is completely destroyed under the control of active normal fault. For the caprock that is not completely

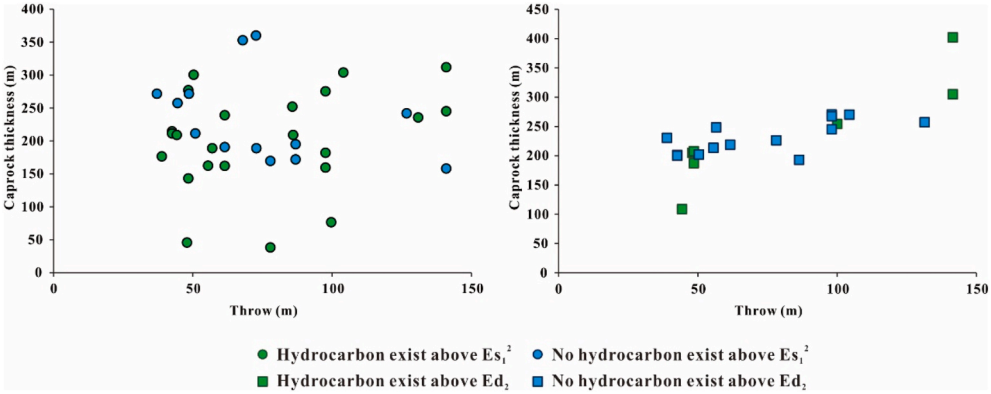

Fig. 19. Scatter plot of fault throws versus caprock thickness. The abscissa is the fault throw, which is the throw during the deposition of the Nm.

destroyed, the thickness of the caprock that functions as a barrier is no longer the original caprock thickness, but the thickness of the juxtaposition caprock. As shown in Fig. 20, the caprock with a thickness of H_c is partially destroyed by a normal fault with a fault throw of H_f. We define the thickness of the juxtaposition caprock as the effective caprock thickness (H_e), which is the original caprock thickness minus the fault throw value, as follows:

$$H_e = H_c - H_f \tag{1}$$

where H_e is the effective caprock thickness, m; H_c is the original caprock thickness, m; and H_f is the fault throw, m.

When the caprock is displaced under the action of fault activity, the sealing of the caprock depends on whether the fault zone is impermeable. The filling material of the fault core is mainly from the wall rock, and the material in the fault core in the mudstone-dominated strata is mainly mudstone, with fine grain size and sealing ability (Fu et al., 2019). Then, whether the fault has sealing ability depends on the permeability of the damage zone. In the T-z plot (Fig. 8), the fault throws have a decreasing trend, which means that the fault will eventually become inactive. When the fault is inactive, the fractures formed during the active period are sealed under compaction and cementation, and the damage zone will lose its transmissibility (Bense et al., 2013). The fault is not permeable, and the caprock becomes a barrier. After being destroyed by the fault, the sealing capacity of the effective caprock must be less than that of the original caprock. Although the effective thickness of the caprock does not refer to the original thickness of the caprock, it is consistent with the meaning and characters of the caprock thickness. Undoubtedly, the larger the effective thickness of the caprock is, the stronger its sealing ability should be. The effective caprock thickness calculated according to formula (1) is shown in Table 2.

Taking the effective caprock thickness as the ordinate and the fault throw during the deposition of the Nm as the abscissa, the scatter diagram is drawn according to whether there are oil reservoirs above and below the caprock. For the Es_1^2 caprock, when the effective thickness of the caprock is less than 126 m, oil reservoirs are found above the caprock; when the thickness is greater than 126 m, oil is only found in the fault-block traps under the caprock (Fig. 21A). For the Ed_2 caprock, when the effective thickness of the caprock is less than 101 m, oil reservoirs are found above the caprock; when the thickness is greater than 101 m, the oil reservoirs only exist below the caprock (Fig. 21B). In addition, no oil reservoir is found when the fault throw is less than 39 m in the study area.

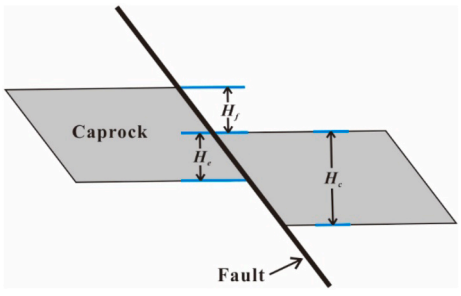

Fig. 20. Schematic diagram of effective caprock thickness.

Although the regional caprock controls the macroscopic distribution of hydrocarbons, the hydrocarbons in the reservoir are still controlled by the local caprock, and the critical hydrocarbon column height needs to be considered. The critical hydrocarbon column height can be calculated using the measured mudstone displacement pressure, but it needs to be converted to the height of the oil column in the actual formation.

The displacement pressure calculated from the mercury intrusion data needs to be converted to the oil displacement pressure in a saturated water environment. For the same rock sample, it can be obtained according to the following formula:

$$P_{do} / P_{dm} = (\sigma_o \cos\theta_o) / (\sigma_m \cos\theta_m) \tag{2}$$

Where P_{do} is the displacement pressure of oil displacement water, MPa; P_{dm} is the displacement pressure of mercury displacement water, MPa; σ_o is the surface tension of oil, mN/m; θ_o is the contact angle of the oil-water-rock interface, °; σ_m is the surface tension of mercury, mN/m; θ_m is the contact angle of the mercury-air-rock interface, °.

The following formula can calculate the critical hydrocarbon column height:

$$P_{do} = (\rho_w - \rho_o) g h_o \tag{3}$$

Where P_{do} is the displacement pressure of oil displacement water, MPa; ρ_w is the density of water, kg/m^3; ρ_o is the density of oil, kg/m^3; g is the gravitational acceleration, m/s$^{2;}$ h_o is the oil column height, m.

We calculated the oil column height by formulas (2) and (3). During the calculation, P_{dm} is the minimum mudstone displacement pressure of 3.81 MPa from Table 3. The data of other parameters in the calculation are from Zhao et al. (2020b). It is calculated that under the minimum mudstone displacement pressure, the critical height of the oil column that can be sealed is about 450 m, while the height of the hydrocarbon column in the study area is far from this height, and the sealing of the caprock is effective.

5.3. Possible accumulation areas

Before the second charging stage, a complete fault plane had been formed, providing a vertical pathway for hydrocarbon migration (Fig. 15). Nevertheless, a large part of the fault has been inactive prior to that period. The permeability of the fault will increase significantly at the beginning of its activity. However, when the fault is inactive, the fracture will close under the compaction of the overlying stratum and

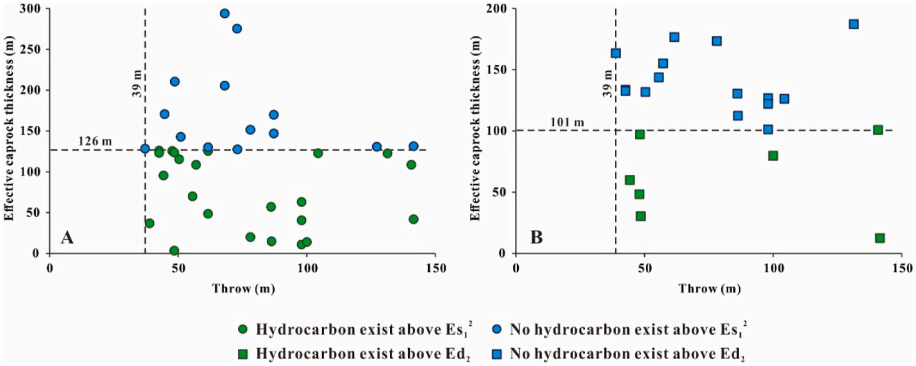

Fig. 21. Scatter plot of fault throws versus effective caprock thickness. The abscissa is the fault throw, which is the throw during the deposition of the Nm.

the mineralisation of the hydrothermal fluid circulation, resulting in a significant decrease in permeability, which in turn cause the fault to lose its conductivity (Bense et al., 2013). The previous analysis found that the fault is reactive in the subsequent evolution, so it is vital whether the reactivation of the fault can make the fault become an effective pathway.

Reactivation of the fault will progressively reduce the grain size of the fault core, resulting in a further decrease in permeability, which will become a barrier to fluid circulation (Brogi, 2008). However, reactivating faults can create new fractures in the fault damage zone, and these fractures are more numerous the closer they are to the fault core (Bauer et al., 2015). The increase in the number of fractures means a greater probability of connectivity between fractures, enhancing permeability and providing pathways for fluid circulation (Brogi, 2008). The damage zone of the reactivated fault can migrate hydrocarbons, while the fault core is impermeable. And when a fault is active or has recently been active, there is a significant increase in permeability, reflected in a higher hydrocarbon production rate, which is verified by the field evidence (Barton et al., 1995). For the fault in the study area, there is indeed a reactivation process, so the damage zone should have the ability to migrate hydrocarbons. At this time, if the source rock is just in the oil window, the reactivation of the fault and the matching of the maturity of the source rock can promote the migration of hydrocarbons.

During the second charge stage, the Es_3^3 source rock reached the gas window, the Es_1^3 source rock reached the oil window, and the Ed_3 source rock generated low-mature oil (Fig. 12). The expulsion of hydrocarbons from the source rock matches the fault reactivation, which helps hydrocarbons migrate along the fault to the overlying traps.

As shown in Fig. 22, the hydrocarbons generated from deep source rocks migrate to the shallow layers through the vertical migration pathway of fault. When the integrity of the caprock is not damaged, and the effective caprock thickness is greater than the lower limit of the thickness, the hydrocarbons can accumulate in the traps under the caprock (the left and right sides of Fig. 22). When the caprock is destroyed under a large fault throw, its ability to seal hydrocarbons is reduced, and the hydrocarbons continue to migrate to shallow layers. Although the existence of the large fault throw causes the integrity of the caprock to be destroyed, a series of reverse drag anticlinal traps are formed, which become favourable places for hydrocarbons to accumulate (the middle of Fig. 22).

For rift basins with mature source rocks, the deep and shallow layers with the large fault throw need to be explored. The deep layer mainly explores reverse drag anticlinal traps, and the shallow target is fault-block traps. Furthermore, the fault-block traps under the effective caprocks are favourable targets for other areas where the continuity of the caprocks have not been destroyed.

6. Conclusions

Based on the study of fault characteristics, charging stages, hydrocarbon distribution characteristics, and the coupling relationship between the regional caprock and the fault throw during the Nm deposition, the following conclusions can be drawn:

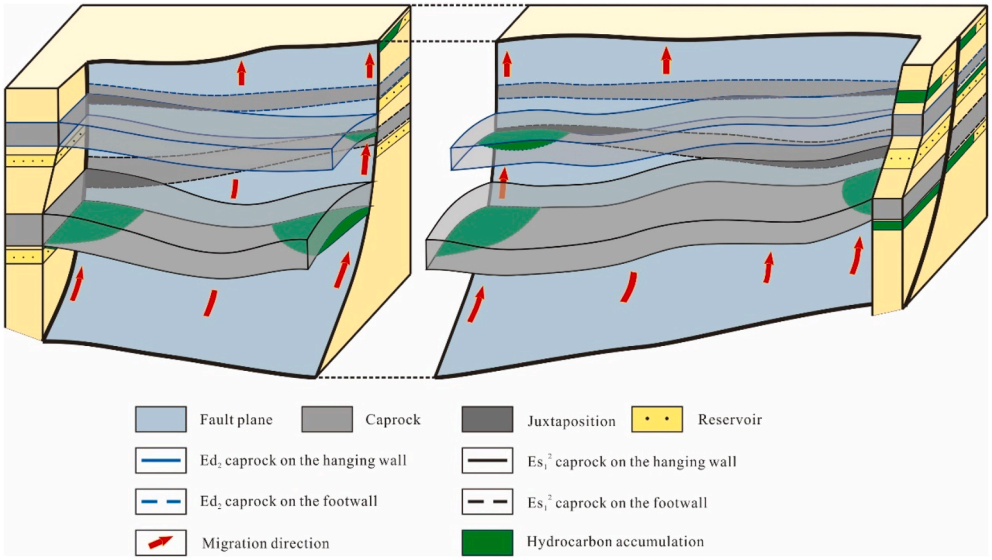

Fig. 22. The model of hydrocarbons migration and distribution along the fault in the study area.

(1) There are differences in the horizontal distribution of faults in the east and west of the study area, which further affects the spatial distribution of hydrocarbons. The western part is controlled by fault F1, and the eastern part is controlled by a series of nearly parallel faults in addition to the control of fault F1.
(2) The fault has undergone the evolution process of lateral and dip linkage, and finally, fault F1 is formed. In the initial stage of the evolution of the fault, there were three isolated faults, and then lateral linkage occurred. Afterwards, there were regional differences in the evolution of the faults. The fault in some areas was blind faults, while the fault in others breached the free surface. After this process, isolated faults developed in the upper part, and then the isolated faults were dipped linkage with the lower existing faults to form a complete fault plane.
(3) Two hydrocarbon charging events occurred in the study area, and the second charging stage is the main stage. The fault had completed dip linkage and reactivated before this period, forming an excellent vertical migration pathway.
(4) Faults and caprocks control the macroscopic distribution of hydrocarbons in the study area. When the effective thickness of Es_1^2 caprock is less than 126 m, and hydrocarbons can be found above the caprock. When the effective thickness of Ed_2 caprock is less than 101 m, hydrocarbons can be found above the Ed_2 caprock. During the deposition of Nm, when the fault throw was not less than 39 m, hydrocarbons were found in the traps near these faults.

Credit author statement

Yuyang Dong: Writing - original draft, Conceptualization, Data curation, Formal analysis, Investigation. **Jianhui Zeng:** Supervision, Funding acquisition, Writing - review & editing. **Xiongying Dong:** Resources, Writing - review & editing. **Chuanming Li:** Formal analysis, Data curation. **Yazhou Liu:** Writing - review & editing.

Declaration of competing interest

The authors declare that they have no known competing financial interests or personal relationships that could have appeared to influence the work reported in this paper.

Acknowledgements

This work was funded by the National Natural Science Foundation of China (Grant No. 41972147). We appreciate the support from the Exploration and Development Research Institute, Dagang Oilfield Company, PetroChina, for providing data and samples used in this study and the permission to publish the results. We thank executive editor Dr. Tahar AÏFA, reviewer Dr. Soumyajit Mukherjee, and anonymous reviewers for their critical and constructive comments that have greatly improved the manuscript.

References

Allan, U.S., 1989. Model for hydrocarbon migration and entrapment within faulted structures. AAPG Bull. 73, 803–811.
Arif, M., Barifcani, A., Lebedev, M., Iglauer, S., 2016. Structural trapping capacity of oil-wet caprock as a function of pressure, temperature and salinity. Int. J. Greenh. Gas Control 50, 112–120.
Bai, B., Lü, G., Li, X., Li, Z., Wang, Y., Hu, Q., 2014. Quantitative measures for characterising the sealing ability of caprock with pore networks in CO_2 geological storage. Energy Proc. 63, 5435–5442.
Barton, C.A., Zoback, M.D., Moos, D., 1995. Fluid flow along potentially active faults in crystalline rock. Geology 23, 683–686.
Baudon, C., Cartwright, J., 2008a. Early stage evolution of growth faults: 3D seismic insights from the Levant Basin, Eastern Mediterranean. J. Struct. Geol. 30, 888–898.
Baudon, C., Cartwright, J.A., 2008b. 3D seismic characterisation of an array of blind normal faults in the Levant Basin, Eastern Mediterranean. J. Struct. Geol. 30, 746–760.
Bauer, J.F., Meier, S., Philipp, S.L., 2015. Architecture, fracture system, mechanical properties and permeability structure of a fault zone in Lower Triassic sandstone, Upper Rhine Graben. Tectonophysics 647, 132–145.
Bense, V., Gleeson, T., Loveless, S., Bour, O., Scibek, J., 2013. Fault zone hydrogeology. Earth Sci. Rev. 127, 171–192.
Boulin, P.F., Bretonnier, P., Vassil, V., Samouillet, A., Fleury, M., Lombard, J.M., 2013. Sealing efficiency of caprocks: experimental investigation of entry pressure measurement methods. Mar. Petrol. Geol. 48, 20–30.
Brogi, A., 2008. Fault zone architecture and permeability features in siliceous sedimentary rocks: insights from the Rapolano geothermal area (Northern Apennines, Italy). J. Struct. Geol. 30, 237–256.
Cartwright, J., Mansfield, C., 1998. Lateral displacement variation and lateral tip geometry of normal faults in the Canyonlands National Park, Utah. J. Struct. Geol. 20 (1), 3–19.
Chen, S., Wang, H., Wu, Y., Huang, C., Wang, J., Xiang, X., Ren, P., 2014. Stratigraphic architecture and vertical evolution of various types of structural slope breaks in Paleogene Qikou sag, Bohai Bay Basin, Northeastern China. J. Petrol. Sci. Eng. 122, 567–584.
Childs, C., Nicol, A., Walsh, J.J., Watterson, J., 2003. The growth and propagation of synsedimentary faults. J. Struct. Geol. 25 (4), 633–648.
Cong, F., Zhang, H., Hao, F., Xu, S., 2020. Direct Control of Normal Fault in Hydrocarbon Migration and Accumulation in Northwestern Bozhong Subbasin, Bohai Bay Basin, China. Marine and Petroleum Geology, 104555.
Corrado, S., Aldega, L., Celano, A.S., De Benedetti, A.A., Giordano, G., 2014. Cap rock efficiency and fluid circulation of natural hydrothermal systems by means of XRD on clay minerals (Sutri, Northern Latium, Italy). Geothermics 50, 180–188.
Dasgupta, S., Biswas, M., Mukherjee, S., Chatterjee, R., 2022. Structural evolution and sediment depositional system along the transform margin- Palar–Pennar basin, Indian east coast. J. Petrol. Sci. Eng., 110155
Deng, H., McClay, K., Bilal, A., 2021. Multiphase activation of the boundary fault system of the eastern Dampier subbasin, Northwest Shelf of Australia. AAPG (Am. Assoc. Pet. Geol.) Bull. 105, 157–188.
Duffy, O.B., Bell, R.E., Jackson, C.A.L., Gawthorpe, R.L., Whipp, P.S., 2015. Fault growth and interactions in a multiphase rift fault network: horda Platform, Norwegian North Sea. J. Struct. Geol. 80, 99–119.
Ferrill, D.A., Evans, M.A., McGinnis, R.N., Morris, A.P., Smart, K.J., Lehrmann, D., Gulliver, K.D.H., Sickmann, Z., 2020. Fault zone processes and fluid history in Austin Chalk, southwest Texas. AAPG (Am. Assoc. Pet. Geol.) Bull. 104, 245–283.
Fossen, H., 2020. Chapter 8 - fault classification, fault growth and displacement. In: Scarselli, N., Adam, J., Chiarella, D., Roberts, D.G., Bally, A.W. (Eds.), Regional Geology and Tectonics, second ed. Elsevier, pp. 119–147.
Fu, G., Wang, Q., Shi, J., 2012. Sealing oil-gas time and ability effectiveness of mudstone caprocks in middle Es_1 in Dagang Oilfield (In Chinese with English abstract). J. Cent. S. Univ. 43 (8), 3142–3148.
Fu, X., Yan, L., Meng, L., Liu, X., 2019. Deformation mechanism and vertical sealing capacity of fault in the mudstone caprock. J. Earth Sci. 30, 367–375.
Gudmundsson, A., Berg, S.S., Lyslo, K.B., Skurtveit, E., 2001. Fracture networks and fluid transport in active fault zones. J. Struct. Geol. 23, 343–353.
Guo, X., Liu, K., Jia, C., Song, Y., Zhao, M., Lu, X., 2016. Effects of early petroleum charge and overpressure on reservoir porosity preservation in the giant Kela-2 gas field, Kuqa depression, Tarim Basin, northwest China. AAPG (Am. Assoc. Pet. Geol.) Bull. 100, 191–212.
Górniak, K., 2019. The cap rocks sealing the reservoir in the Węglówka oil field, sub-Silesian unit, Polish outer Carpathians: petrographical approach. AAPG (Am. Assoc. Pet. Geol.) Bull. 103, 2369–2398.
Hansberry, R.L., King, R.C., Holford, S.P., Hand, M., Debenham, N., 2021. How wide is a fault damage zone? Using network topology to examine how fault-damage zones overprint regional fracture networks. J. Struct. Geol. 146.
Hao, F., Zhou, X., Zhu, Y., Zou, H., Bao, X., Kong, Q., 2009. Mechanisms of petroleum accumulation in the Bozhong sub-basin, Bohai Bay Basin, China. Part 1: origin and occurrence of crude oils. Mar. Petrol. Geol. 26, 1528–1542.
Hu, M., Fang, J., Zhao, J., Yao, Z., Wang, X., 2019. Characteristics and main accumulation controlling factors for deep hydrocarbon reservoirs in Madong area of Qikou Sag (In Chinese with English abstract). Pet. Geol. Oilfield Dev. Daqing 38 (6), 32–39.
Hooper, E., 1991. Fluid migration along growth faults in compacting sediments. J. Petrol. Geol. 14, 161–180.
Ito, D., Akaku, K., Okabe, T., Takahashi, T., Tsuji, T., 2011. Measurement of threshold capillary pressure for seal rocks using the step-by-step approach and the residual pressure approach. Energy Proc. 4, 5211–5218.
Jackson, C.A.L., Rotevatn, A., 2013. 3D seismic analysis of the structure and evolution of a salt-influenced normal fault zone: a test of competing fault growth models. J. Struct. Geol. 54, 215–234.
Jin, Z., Yuan, Y., Sun, D., Liu, Q., Li, S., 2014. Models for dynamic evaluation of mudstone/shale cap rocks and their applications in the Lower Paleozoic sequences, Sichuan Basin, SW China. Mar. Petrol. Geol. 49, 121–128.
Kawaura, K., Akaku, K., Nakano, M., Ito, D., Takahashi, T., Kiriakehata, S., 2013. Examination of methods to measure capillary threshold pressures of pelitic rock samples. Energy Proc. 37, 5411–5418.
Kim, Y.S., Andrews, J.R., Sanderson, D.J., 2001. Reactivated strike-slip faults: examples from north Cornwall, UK. Tectonophysics 340 (3–4), 173–194.
Kim, Y.S., Sanderson, D.J., 2005. The relationship between displacement and length of faults: a review. Earth Sci. Rev. 68 (3), 317–334.
Krooss, B.M., Leythaeuser, D., 1997. Diffusion of methane and ethane through the reservoir cap rock: implications for the timing and duration of catagenesis: discussion. AAPG (Am. Assoc. Pet. Geol.) Bull. 81 (1), 155–161.

Lathrop, B.A., Jackson, C.A.L., Bell, R.E., Rotevatn, A., 2021. normal fault kinematics and the role of lateral tip retreat: an example from offshore NW Australia. Tectonics 40 (5).
Ma, C., Lin, C., Dong, C., Luan, G., Zhang, Y., Sun, X., Liu, X., 2019. Quantitative relationship between argillaceous caprock thickness and maximum sealed hydrocarbon column height. Nat. Resour. Res. 29, 2033–2049.
Mattos, N.H., Alves, T.M., Omosanya, K.O., 2016. Crestal fault geometries reveal late halokinesis and collapse of the Samson Dome, Northern Norway: implications for petroleum systems in the Barents Sea. Tectonophysics 690, 76–96.
Maunde, A., Alves, T.M., 2022. Effect of tectonic inversion on supra-salt fault geometry and reactivation histories in the Southern North Sea. Mar. Petrol. Geol. 135, 105401.
McCulloh, R.P., 1988. Differential fault-related early Miocene sedimentation, Bayou Hebert area, southwestern Louisiana. AAPG Bull. 72, 477–492.
Misra, A.A., Mukherjee, S., 2018. Atlas of Structural Geological Interpretation from Seismic Images. John Wiley & Sons.
Muraoka, H., Kamata, H., 1983. Displacement distribution along minor fault traces. J. Struct. Geol. 5, 483–495.
Nabavi, S.T., Fossen, H., 2021. Fold geometry and folding–a review. Earth Sci. Rev. 103812.
Nicol, A., Watterson, J., Walsh, J., Childs, C., 1996. The shapes, major axis orientations and displacement patterns of fault surfaces. J. Struct. Geol. 18, 235–248.
Pochat, S., Castelltort, S., Choblet, G., Van Den Driessche, J., 2009. High-resolution record of tectonic and sedimentary processes in growth strata. Mar. Petrol. Geol. 26, 1350–1364.
Pu, X., Zhou, L., Wang, W., Han, W., Xiao, D., Liu, H., Chen, C., Zhang, W., Yuan, X., Lu, Y., Liu, S., 2013. Medium-deep clastic reservoirs in the slope area of Qikou sag, Huanghua depression, Bohai Bay Basin. Petrol. Explor. Dev. 40 (1), 36–48.
Pu, X., Zhou, L., Han, Wen, Chen, C., Yuan, X., Lin, C., Liu, S., Han, G., Zhang, W., Jiang, W., 2014. Gravity flow sedimentation and tight oil exploration in lower first member of Shahejie Formation in slope area of Qikou Sag, Bohai Bay Basin. Petrol. Explor. Dev. 41 (2), 138–149.
Schlömer, S., Krooss, B., 1997. Experimental characterisation of the hydrocarbon sealing efficiency of cap rocks. Mar. Petrol. Geol. 14, 565–580.
Schmitt, M., Poffo, C.M., de Lima, J.C., Fernandes, C.P., dos Santos, V.S.S., 2017. Application of photoacoustic spectroscopy to characterise thermal diffusivity and porosity of caprocks. Eng. Geol. 220, 183–195.
Smith, D.A., 1966. Theoretical considerations of sealing and non-sealing faults. AAPG (Am. Assoc. Pet. Geol.) Bull. 50 (2), 363–374.
Tao, Z., Alves, T.M., 2019. Impacts of data sampling on the interpretation of normal fault propagation and segment linkage. Tectonophysics 762, 79–96.
Thorsen, C.E., 1963. Age of growth faulting in southeast Louisiana. Gulf Coast Association of Geological Societies Transactions 13, 103–110.
Tvedt, A.B.M., Rotevatn, A., Jackson, C.A.L., Fossen, H., Gawthorpe, R.L., 2013. Growth of normal faults in multilayer sequences: a 3D seismic case study from the Egersund Basin, Norwegian North Sea. J. Struct. Geol. 55, 1–20.
Volk, H., George, S.C., 2019. Using petroleum inclusions to trace petroleum systems–A review. Org. Geochem. 129, 99–123.
Walsh, J., Bailey, W., Childs, C., Nicol, A., Bonson, C., 2003. Formation of segmented normal faults: a 3-D perspective. J. Struct. Geol. 25, 1251–1262.
Wang, C., Zeng, J., Yu, Y., Cai, W., Li, D., Yang, G., Liu, Y., Wang, Z., 2020. Origin, migration, and characterisation of petroleum in the perdido fold belt, gulf of Mexico basin. J. Petrol. Sci. Eng. 195, 107843.
Wang, W., Pang, X., Chen, Z., Chen, D., Wang, Y., Wang, W., Luo, B., Zhang, W., Zhang, X., Li, C., 2021. Quantitative Evaluation of Transport Efficiency of Fault-Reservoir Composite Migration Pathway Systems in Carbonate Petroliferous Basins. Energy, p. 119983.
Wang, Z., Hua, S., Yu, X., Jiang, W., 2014. Grading evaluation and high quality source rock distribution in Qikou Sag (In Chinese with English abstract). Nat. Gas Geosci. 25 (12), 1896–1902.
Watts, N.L., 1987. Theoretical aspects of cap-rock and fault seals for single-and two-phase hydrocarbon columns. Mar. Petrol. Geol. 4 (4), 274–307.
Wibberley, C.A., Yielding, G., Di Toro, G., 2008. Recent advances in the understanding of fault zone internal structure: a review. Geological Society, London, Special Publications 299, 5–33.
Wu, J., Fan, T., Gomez-Rivas, E., Gao, Z., Yao, S., Li, W., Zhang, C., Sun, Q., Gu, Y., Xiang, M., 2019. Impact of pore structure and fractal characteristics on the sealing capacity of Ordovician carbonate cap rock in the Tarim Basin, China. Mar. Petrol. Geol. 102, 557–579.
Xu, S., Hao, F., Xu, C., Zou, H., Quan, Y., 2016. Oil migration through preferential petroleum migration pathway (PPMP) and polycyclic faults: a case study from the Shijiutuo Uplift, Bohai Bay Basin, China. Mar. Petrol. Geol. 73, 539–553.
Xu, S., Hao, F., Xu, C., Zou, H., Zhang, X., Zong, Y., Zhang, Y., Cong, F., 2019. Hydrocarbon migration and accumulation in the northwestern Bozhong subbasin, Bohai Bay Basin, China. J. Petrol. Sci. Eng. 172, 477–488.
Yu, C., Su, J., Qian, M., Gao, S., Xiao, M., Zhao, S., Liu, X., 2010. Distribution and controlling factors of Eogene oil & gas reservoirs in Binhai fault nose zone (In Chinese with English abstract). Nat. Gas Geosci. 21 (4), 547–553.
Zhang, L., Bai, G., Zhao, X., Zhou, L., Zhou, S., Jiang, W., Wang, Z., 2019. Oil-source correlation in the slope of the Qikou depression in the Bohai Bay Basin with discriminant analysis. Mar. Petrol. Geol. 109, 641–657.
Zhao, X., Jin, F., Li, Y., Wang, Q., Zhou, L., Lyu, Y., Pu, X., Wang, W., 2016. Slope belt types and hydrocarbon migration and accumulation mechanisms in rift basins. Petrol. Explor. Dev. 43 (6), 841–849.
Zhao, X., Pu, X., Zhou, L., Xiao, D., Chen, C., Han, W., Zhang, W., Shi, Z., Lin, C., Yang, F., 2017. Reconstruction of Paleogene sedimentary system and reservoir evaluation in Qikou sag, Bohai Bay Basin, China (in Chinese with English abstract). J. Chengdu Univ. Technol. (Sci. Technol. Ed.) 44 (5), 565–578.
Zhao, X., Zhou, L., Pu, X., Shi, Z., Han, G., Wu, J., Han, W., Zhang, W., Gao, H., Ma, J., Wang, H., 2020a. Geological characteristics and exploration breakthrough of shale oil in Member 3 of Shahejie Formation of Qibei subsag, Qikou sag. Acta Pet. Sin. 41 (6), 643–657.
Zhao, X., Zeng, J., Han, G., Feng, S., Shi, Q., Liu, Y., Fu, D., Wang, Y., Zong, J., Lu, Y., 2020b. Charging characteristics and accumulation process of deep low – permeability (tight) sand gas reservoirs in Banqiao Sag, Huanghua Depression (In Chinese with English abstract). Oil Gas Geol. 41 (5), 913–927.
Zhou, L., Han, G., Dong, Y., Shi, Q., Ma, J., Hu, J., Ren, S., Zhou, K., Wang, J., Si, W., 2019. fault-sand combination modes and hydrocarbon accumulation in Binhai fault nose of Qikou sag, Bohai Bay Basin, east China. Petrol. Explor. Dev. 46 (5), 869–882.
Yu, X., He, Y., Jiang, W., Liu, Q., Liang, B., Zou, L., 2011. Hydrocarbon generation of Paleogene source rocks in Qikou sag (In Chinese with English abstract). Nat. Gas Geosci. 22 (6), 1001–1008.